This is to certify that the

thesis entitled

Elastic and Inelastic Scattering of ^{6}Li from ^{58}Ni

presented by

Cecil L. Williamson

has been accepted towards fulfillment
of the requirements for

__Masters__ degree in __Physics__

Aaron Galonsky
Major professor

Date__June 6, 1979__

O-7639

OVERDUE FINES ARE 25¢ PER DAY
PER ITEM

Return to book drop to remove
this checkout from your record.

MSU

ELASTIC AND INELASTIC SCATTERING OF ^{6}Li FROM ^{58}Ni

By

Cecil L. Williamson

A THESIS

Submitted to
Michigan State University
in partial fulfillment of the requirements
for the degree of

MASTER OF SCIENCE

Department of Physics

1979

ABSTRACT

ELASTIC AND INELASTIC SCATTERING OF ^{6}Li FROM ^{58}Ni

By

Cecil L. Williamson

Elastic scattering of ^{6}Li from ^{58}Ni at 73.4 MeV was studied, and five sets of optical model parameters were obtained which gave equivalently good fits to the data. These data were gathered using surface-barrier detectors in a forty-inch diameter scattering chamber.

Nine inelastic states of ^{58}Ni were studied via the same reaction at 71.2 MeV. These data were gathered using a position-sensitive proportional counter placed in the focal plane of a split-pole spectrograph. Two methods were employed to analyze the data. They were the distorted wave Born approximation (DWBA), and the method of coupled channels. A comparison of these methods and the information they provide about the nuclear deformation lengths is presented. It was anticipated that comparison of the experimental inelastic angular distributions with theoretical predictions would produce an unambiguous choice of optical model parameters to describe the elastic scattering process. This was not possible, however, because each set of parameters gave equally good fits to the data.

TABLE OF CONTENTS

Page

LIST OF TABLES

LIST OF FIGURES

1. INTRODUCTION

The complex optical model potential has been used for
many years in the successful reproduction of elastic scatter-
ing angular distributions. Usually, several sets of optical
model (OM) parameters may be found to fit experimental angu-
lar distributions over the range for which data are gathered.
It is not frequently possible, however, to make a conclusive
statement indicating that a particular set of OM parameters
gives the most accurate description of an interaction. This
may be due to the interdependent nature of the parameters or
it may simply be a property of the potential.

Optical model analysis has also been logically extended
to the treatment of the inelastic scattering process and has
been employed to provide information on nuclear shapes. This
process is usually treated as a direct transition from the
ground state involving only the first derivative of the OM.
Also, it is most common to assume that the wavefunction
describing the projectile has the same form following an
interaction as it had prior to the interaction. This last
assumption is a part of the distorted wave Born approximation
(DWBA). With the advent of high speed computers in the mid-
1950's, implementation of these assumptions into a machine
code has led to generally successful studies of the inelastic
scattering of many projectiles with a wide variety of
energies from most known stable nuclei.

Advances in speed and efficiency of computers have made possible more comprehensive approximations of the scattering processes. In particular, indirect transitions which may occur via multistep processes may now be treated directly in the codes by use of the coupled channels method of analysis. In this type of analysis, it is possible for any transition to a final state (or channel) to affect transitions to any other state through the coupled system of equations which describes the interaction. Coupled channels (CC) calculations of this type for the higher excited states of low lying collective bands have proven quite successful in providing improved fits to data when the DWBA was deemed inadequate.

DWBA for nine inelastic states and CC for the first vibrational band have been herein employed to describe ^{6}Li scattering from ^{58}Ni at a lab energy of 71.2 MeV. The nuclear deformation lengths extracted are compared to previously determined values and the fits to the data provided by each method are compared and contrasted.

2. INELASTIC SCATTERING OF ^{6}Li FROM ^{58}Ni AT 71.2 MeV

2.1. Introduction

Elastic[1-5] and inelastic[3,4] scattering of ^{6}Li by medium weight nuclei have been studied recently, but none of the studies has investigated inelastic transitions in ^{58}Ni with projectile energies above 34 MeV. In the present work nine inelastic transitions were observed in ^{58}Ni at 71 MeV. Each transition was treated as a one-phonon collective transition in the DWBA using complex coupling. Since the deformations of separate portions of the interaction potential (real, imaginary, Coulomb) need not necessarily be equal, the calculations were performed twice with each set of optical model parameters which fit the elastic scattering data.[5] In one set of calculations, the deformations were held equal, and in the other set of calculations, the deformation lengths were held equal.

Preliminary coupled-channels calculations were also performed for the lowest energy, 0^+-2^+-4^+, vibrational band which coupled the ground state and first two excited states. Investigations into multiple-plus-direct with admixtures of one- and two-phonon transitions for the first 4^+ state at 2.45 MeV were performed with α-particle scattering as early as 1962 by Buck[6] and as recently as 1972 by Horen et al.[7] These studies were prompted by the fact that this state does not follow the Blair phase rule. According to this rule,

angular distributions corresponding to even values of angular momentum transfer L should be out of phase with angular distributions corresponding to odd L transfer. Also, angular distributions with odd L should be in phase with the elastic distributions.

For the ^{90}Zr + ^{6}Li reaction at 34 MeV[3] and 75 MeV,[8] sizable differences have been noted between extracted deformation lengths and previously reported values. Anticipation of these observations was one motivation in performing this investigation.

2.2. Experimental Procedures

The MSU sector-focused cyclotron was used to produce an extracted beam of 200-300 nA of ^{6}Li^{+++} ions. An arc-type ion source[9] produced the beam through the sputtering action of Ne on LiFl pellets, enriched in ^{6}Li. Electrodes of tantalum (source life, approximately three hours) were used, but hafnium was briefly employed in an attempt to increase source life.[10] (Hafnium did increase source lifetime by approximately a factor of two, but on-target current was reduced by a factor of approximately four.) Two analyzing magnets and several quadrupole focusing magnets were used to give a rectangular beam spot of approximately 2 mm x 4 mm on a foil target of 1.02 mg/cm^2, 99% enriched ^{58}Ni. On-target beam intensity of 10—50 nA at 71.2 MeV was monitored by stopping the beam in a Faraday cup and sending the current to an Ortec charge digitizer for charge measurement.

A detector with two resistive-wire, proportional counters[11] in sequence backed by a scintillator, placed in the focal plane of an Enge split-pole spectrograph was used to gather the data. Two-dimensional gating techniques (ΔE vs. TOF (time-of-flight), ΔE vs. position, TOF vs. position, and light vs. position) were used for multiple identification of the scattered lithium ions. A PDP-11/45 on-line computer was used for gating, display, and collection of data. A block diagram of the apparatus is shown in Figure 1.

The low beam intensity restricted the range over which it was possible to gather data to lab angles less than approximately 45°. A FWHM $\simeq$ 90 keV made it possible to resolve nine inelastic states. Typical spectra are displayed in Figure 2. The data were normalized using the 74 MeV elastic scattering results of Huffman et al.[5] gathered at the MSU Heavy Ion Lab using a 40-inch scattering chamber equipped with two telescope-mounted ΔE–E silicon surface-barrier detector pairs. The optical model parameter set of Table 2 with V = 160 MeV was used to calculate the elastic scattering at E_{LAB} = 71 MeV. The data of this experiment for which elastic scattering was observed ($\theta_{cm} \gtrsim 18^{\circ}$) were then normalized to this angular distribution. For angles below 18°, the elastic peak was not recorded (see upper spectrum of Figure 2) in order to decrease dead-time in the detector. The magnitude of the correction required to obtain normalization of the data was significant mostly for angles greater

Figure 1. Block diagram of the apparatus for the inelastic scattering experiment. F → Front, B → Back, DYN → Dynode, AN → Anode, FC → Faraday Cup, TC → Timer-Counter, CD → Current Digitizer, PA → Preamp, DISC → Discriminator, PS → Pulse Shaper, TSCA → Timing Single Channel Analyzer, TAC → Time-Analog Converter, G&D → Gate and Delay, SC → Scalar.
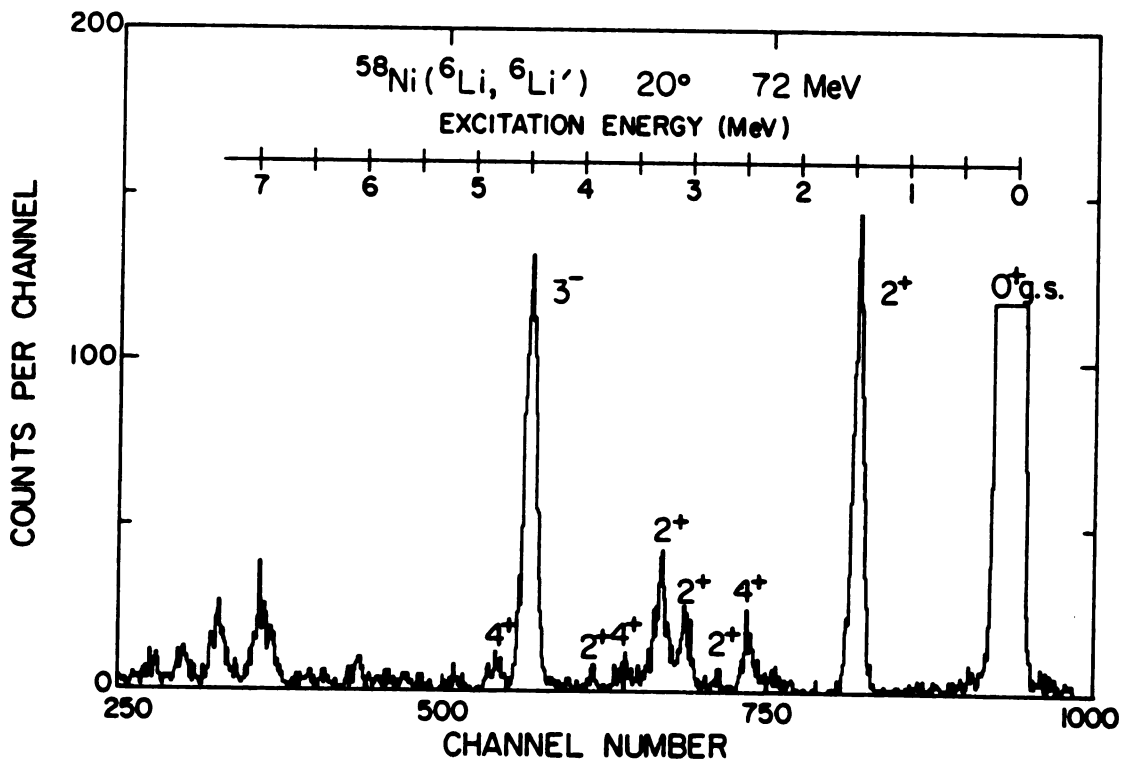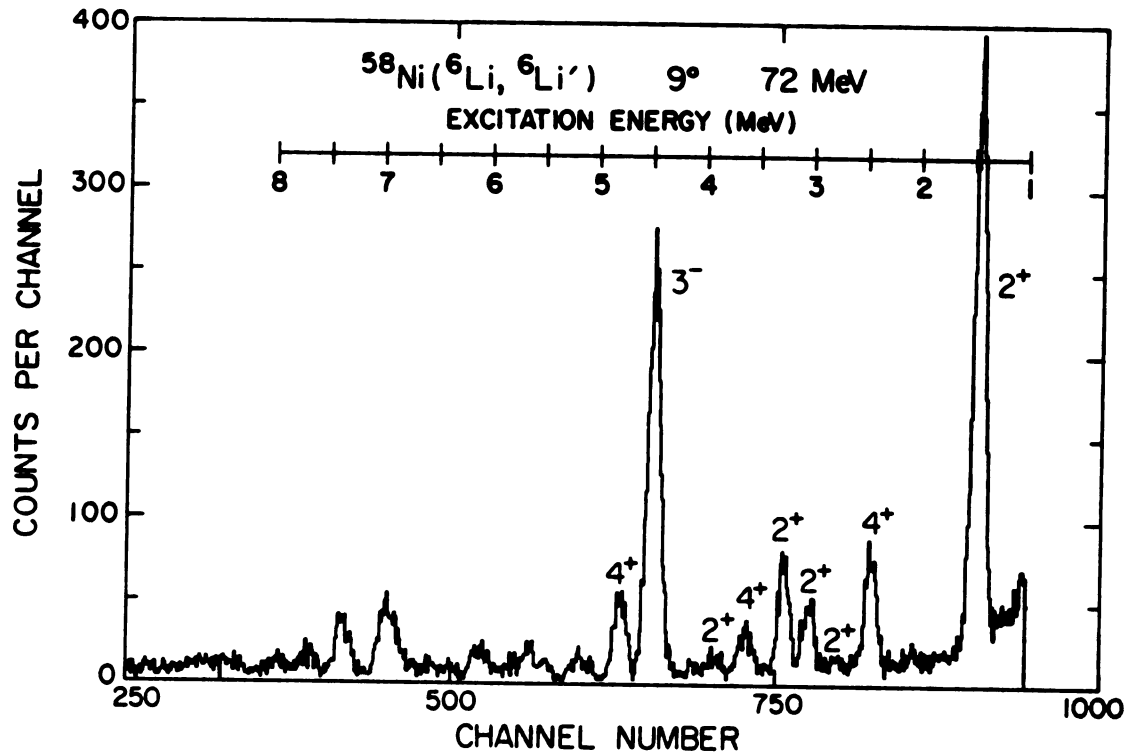
Figure 2. Typical spectra for the inelastic scattering experiment. The elastic peak is cut off for clarity in the 20° spectrum.

Table 1. Data from the 71.2 MeV experiment. The cross sections and uncertainties are in mb/sr unless otherwise specified.

	Elastic			1.4540 MeV 2^+	
θ_{cm}	$d\sigma/d\Omega$	$\Delta\sigma$ (%)	θ_{cm}	$d\sigma/d\Omega$	$\Delta\sigma$
18.594	486.4	0.3	8.681	3.418E 01	5.811E-01
19.695	286.2	0.3	9.786	1.540E 01	3.080E-01
20.794	201.5	0.3	10.891	1.875E 01	4.313E-01
21.893	159.6	0.3	11.995	3.330E 01	4.329E-01
22.992	177.8	0.4	13.100	4.592E 01	1.240E 00
24.090	73.9	0.6	14.203	2.917E 01	3.792E-01
25.187	41.5	0.9	15.307	1.182E 01	3.073E-01
26.283	26.0	0.8	16.410	6.482E 00	1.750E-01
27.379	21.3	0.6	17.512	1.197E 01	2.154E-01
28.474	18.7	0.7	18.614	1.638E 01	2.293E-01
30.662	8.38	1.1	19.715	1.259E 01	1.763E-01
32.846	2.89	2.9	20.816	5.374E 00	1.075E-01
35.026	2.73	1.7	21.916	2.255E 00	6.314E-02
37.203	1.19	3.2	23.016	2.451E 00	6.373E-02
39.375	0.275	7.9	24.115	4.249E 00	1.105E-01
41.544	0.433	3.8	25.213	5.080E 00	1.321E-01
			26.311	3.146E 00	7.237E-02
			27.408	1.062E 00	2.973E-02
			28.504	4.064E-01	1.829E-02
			30.693	1.156E 00	4.507E-02
			32.880	1.024E 00	4.916E-02
			35.062	9.920E-02	8.928E-03
			37.241	2.339E-01	1.661E-02
			39.415	2.656E-01	2.125E-02
			41.585	2.678E-02	4.017E-03

Table 1 (cont'd).

	2.4591 MeV 4$^+$			2.7753 MeV 2$^+$	
θ_{cm}	$d\sigma/d\Omega$	$\Delta\sigma$	θ_{cm}	$d\sigma/d\Omega$	$\Delta\sigma$
8.688	3.517E 00	2.550E-01	8.690	2.719E-01	1.493E-01
9.794	3.973E 00	2.900E-01	9.796	3.646E-01	7.908E-02
10.899	3.409E 00	1.704E-01	10.902	5.794E-01	7.068E-02
12.005	2.033E 00	1.078E-01			
13.110	1.042E 00	6.356E-02	13.113	2.263E-01	2.964E-02
14.214	4.936E-01	4.788E-02	14.218	1.908E-01	3.053E-02
15.318	8.353E-01	8.019E-02	15.322	8.185E-02	2.619E-02
16.422	1.150E 00	7.244E-02	16.426	6.868E-02	1.346E-02
17.525	1.088E 00	6.635E-02	17.529	5.596E-02	1.567E-02
18.628	1.099E 00	5.606E-02	18.632	6.747E-02	1.471E-02
19.730	2.042E-01	2.246E-02	19.735	2.997E-01	4.256E-02
20.832	1.989E-01	1.989E-02	20.837	1.347E-01	1.697E-02
21.933	2.996E-01	2.307E-02	21.938	4.962E-02	9.378E-03
23.033	4.079E-01	2.652E-02	23.039	3.384E-02	7.579E-03
24.133	3.440E-01	3.302E-02	24.139	2.057E-02	7.817E-03
25.232	1.572E-01	2.357E-02	25.238	2.005E-02	8.182E-03
26.330	4.661E-02	8.856E-03	26.337	1.285E-02	4.498E-03
27.428	4.536E-02	5.897E-03	27.435	2.672E-02	4.542E-03
28.525	1.047E-01	9.215E-03	28.532	2.434E-02	4.454E-03
30.716	8.857E-02	8.857E-03	30.723	9.126E-03	2.920E-03
32.904	1.661E-02	7.974E-04	32.911	2.372E-03	2.372E-03
35.088	3.487E-02	5.928E-03	35.096	7.922E-03	2.535E-03
37.268	2.490E-02	5.478E-03	37.276	2.371E-03	5.215E-04
39.444	6.769E-03	3.379E-03	39.453	3.378E-03	2.381E-03
41.615	8.511E-03	2.298E-03	41.625	3.646E-03	1.495E-03

Table 1 (cont'd).

θ_{cm}	3.0378 MeV 2^+		θ_{cm}	3.2635 MeV 2^+	
	$d\sigma/d\Omega$	$\Delta\sigma$		$d\sigma/d\Omega$	$\Delta\sigma$
8.692	2.849E 00	2.191E-01	8.693	3.921E 00	2.443E-01
9.798	1.875E 00	1.204E-01	9.800	3.084E 00	1.375E-01
10.904	2.031E 00	1.320E-01	10.906	2.765E 00	1.549E-01
12.010	2.405E 00	1.154E-01	12.012	3.224E 00	1.354E-01
13.115	3.749E 00	1.575E-01	13.118	4.779E 00	1.673E-01
14.220	2.694E 00	1.104E-01	14.223	3.511E 00	1.264E-01
15.325	1.497E 00	1.108E-01	15.328	1.971E 00	1.281E-01
16.429	7.186E-01	5.749E-02	16.432	1.066E 00	7.036E-02
17.533	8.631E-01	5.869E-02	17.536	8.148E-01	5.704E-02
18.636	1.314E 00	6.436E-02	18.639	1.445E 00	6.790E-02
19.739	1.167E 00	5.487E-02	19.742	1.492E 00	6.267E-02
20.841	9.832E-01	7.866E-02	20.845	9.694E-01	8.628E-02
21.943	3.937E-01	2.559E-02	21.946	6.564E-01	3.217E-02
23.043	1.708E-01	1.708E-02	23.047	2.046E-01	1.862E-02
24.144	2.703E-01	2.973E-02	24.148	2.907E-01	2.907E-02
25.243	4.110E-01	3.699E-02	25.247	4.642E-01	3.946E-02
26.342	3.035E-01	2.216E-02	26.346	4.912E-01	2.800E-02
27.440	1.441E-01	1.081E-02	27.445	2.031E-01	1.280E-03
28.537	5.758E-02	6.853E-03	28.542	1.062E-01	9.347E-03
30.729	5.748E-02	7.472E-03	30.734	8.117E-02	8.928E-03
32.918	9.960E-02	1.494E-02	32.923	1.329E-01	1.861E-02
35.103	2.930E-02	4.688E-03	35.108	3.800E-02	5.320E-03
37.283	8.295E-03	3.152E-03	37.290	9.476E-03	3.317E-03
39.460	2.195E-02	6.146E-03	39.467	2.363E-02	6.381E-03
41.632	9.112E-03	2.369E-03	41.639	1.579E-02	3.158E-03

Table 1 (cont'd).

θ_{cm}	3.6204 MeV 4+ $d\sigma/d\Omega$	$\Delta\sigma$	θ_{cm}	3.8985 MeV 2+ $d\sigma/d\Omega$	$\Delta\sigma$
8.696	1.428E 00	1.756E-01	8.697	6.932E-01	1.476E-01
9.802	1.562E 00	1.025E-01	9.805	8.626E-01	7.703E-02
10.909	1.788E 00	1.001E-01	10.911	1.114E 00	9.911E-02
12.015	1.538E 00	9.381E-02	12.018	1.068E 00	7.797E-02
13.121	1.032E 00	6.339E-02	13.124	1.102E 00	6.392E-02
14.227	4.509E-01	4.509E-02	14.230	6.226E-01	5.292E-02
15.332	3.679E-01	5.481E-02	15.335	3.268E-01	5.229E-02
16.437	5.259E-01	4.891E-02	16.440	2.788E-01	3.346E-02
17.541	6.348E-01	5.015E-02	17.545	2.833E-01	3.400E-02
18.645	5.647E-01	4.221E-02	18.649	3.496E-01	3.286E-02
19.748	2.993E-01	2.904E-02	19.752	2.476E-01	2.476E-02
20.850	1.260E-01	1.638E-02	20.855	1.345E-01	1.613E-02
21.952	1.345E-01	1.480E-02	21.957	8.492E-02	1.223E-02
23.054	2.163E-01	1.960E-02	23.059	1.182E-01	1.419E-02
24.154	2.084E-01	2.730E-02	24.160	1.291E-01	1.937E-02
25.254	1.736E-01	2.430E-02	25.260	8.343E-02	1.669E-02
26.354	8.825E-02	1.191E-02	26.359	4.812E-02	9.143E-03
27.452	7.197E-02	7.917E-03	27.458	3.153E-02	5.044E-03
28.550	5.510E-02	6.667E-03			
30.743	6.928E-02	7.967E-03	30.749	2.278E-02	4.556E-03
32.932	2.606E-02	2.606E-03	32.939	1.421E-02	5.827E-03
35.118	3.165E-03	1.583E-03	35.125	5.537E-03	2.104E-03
37.300	1.302E-02	3.933E-03			
39.477	1.012E-02	4.150E-03	39.485	3.373E-03	2.361E-03
41.650	1.821E-03	1.056E-03	41.659	1.214E-03	8.496E-04

Table 1 (cont'd.).

| θ_{cm} | 4.475 MeV 3^- | | θ_{cm} | 4.754 MeV 4^+ | |
	$d\sigma/d\Omega$	$\Delta\sigma$		$d\sigma/d\Omega$	$\Delta\sigma$
8.701	1.852E 01	4.094E-01	8.703	2.167E 00	1.788E-01
9.809	1.309E 01	2.473E-01	9.811	2.616E 00	1.190E-01
10.916	9.143E 00	2.834E-01	10.919	2.586E 00	1.500E-01
12.024	5.867E 00	1.819E-01	12.026	2.037E 00	1.080E-01
13.130	8.144E 00	1.792E-01	13.133	1.369E 00	7.255E-02
14.237	8.184E 00	1.964E-01	14.240	7.331E-01	5.865E-02
15.342	7.935E 00	2.539E-01	15.346	7.181E-01	7.899E-02
16.448	6.060E 00	1.636E-01	16.451	7.303E-01	5.770E-02
17.553	3.269E 00	1.144E-01	17.557	9.644E-01	6.172E-02
18.657	2.913E 00	9.613E-02	18.661	7.816E-01	5.002E-02
19.761	3.175E 00	8.890E-02	19.765	4.070E-01	3.256E-02
20.864	3.149E 00	8.188E-02	20.869	2.089E-01	2.089E-02
21.967	2.544E 00	6.613E-02	21.972	1.838E-01	1.801E-02
23.069	1.701E 00	5.444E-02	23.074	2.362E-01	2.007E-02
24.171	1.038E 00	5.500E-02	24.176	2.667E-01	2.667E-02
25.271	1.014E 00	5.778E-02	25.277	3.133E-01	3.133E-02
26.371	1.014E 00	4.058E-02	26.377	1.602E-01	1.762E-02
27.470	8.166E-01	2.613E-02	27.476	5.168E-02	6.718E-03
28.569	6.750E-01	2.363E-02	28.575	4.046E-02	5.664E-03
30.763	2.458E-01	1.499E-02	30.770	8.373E-02	8.373E-03
32.954	2.698E-01	2.536E-02	32.961	6.624E-02	1.259E-02
35.141	2.000E-01	1.260E-02	35.148	1.580E-02	3.476E-03
37.324	8.278E-02	9.934E-03	37.332	2.601E-02	5.462E-03
39.503	5.899E-02	1.003E-02	39.511	1.685E-02	5.324E-03
41.677	5.094E-02	5.603E-03	41.686	3.031E-03	1.364E-03

Table 2.   Optical model parameter sets which give the best
fits to the elastic scattering data.

V	r_R	a_R	W	r_I	a_I
60.00	1.4315	.8351	17.5852	1.7828	.7790
110.00	1.2643	.8642	17.9915	1.7720	.7767
160.00	1.1727	.8672	18.7939	1.7577	.7837
225.44	1.0743	.8870	19.9029	1.7444	.7755
295.77	1.0063	.8899	21.5315	1.7210	.7802

than 30°. Therefore, it is assumed that corrections to the small angle data would have been negligible and no further investigations into normalization of the data were performed. The accuracy of the data, unless otherwise specified, is $\pm$ 5% relative with an additional $\pm$ 5% absolute.

2.3 DWBA Analysis

Optical potentials with volume real and volume imaginary terms of the standard Woods-Saxon form were used in DWBA analysis of the data:

$$U(r) = -V \, f(r) - i \, Wg(r)$$

$$\text{where } f(r) = [1 + \exp \, (\frac{r-R_R}{a_R})]^{-1},$$

$$g(r) = [1 + \exp \, (\frac{r-R_I}{a_I})]^{-1}$$

$$\text{and } R_R = r_R A^{1/3}, \; R_I = r_I A^{1/3} \; .$$

Added to this was the potential due to a spherically symmetric, uniform charge distribution of radius R_c.

We used a first-derivative, collective-model form factor, with Coulomb excitation included, to describe the interaction:

$$F(r) = F_D(r) + F_C(r)$$

$$F_D(r) = -[V \, R_R \frac{df(r)}{dr} + i \, W \, R_I \frac{dg(r)}{dr}]$$

$$F_c(r) = \frac{3ZZ'e^2}{(2L+1)} \frac{R_c^L}{r^{(L+1)}}, \quad r > R_c,$$

$$= 0, \quad r < R_c,$$

where $R_c = 1.40 \, A^{1/3}$ fm and L is the angular momentum trans-ferred. Coulomb excitation was significant mostly at small angles.

Calculations of the theoretical differential cross sections were performed on an XDS Σ–7 computer using the code DWUCK 72.[12] In the collective model,

$$\left(\frac{d\sigma_L}{d\Omega}\right)_{Exp} = \beta_L^2 \left(\frac{d\sigma}{d\Omega}\right)_{Th}.$$

Implicit in this model is the assumption that the deformation parameter β_L applies equally to the real, absorptive, and Coulomb terms in the potential, i.e. $\beta_{LR} = \beta_{LI} = \beta_{LC}$. However, by appropriate scaling of V, W, and the Coulomb excitation scale factor, it is possible to set the deforma-tion lengths $\delta_L = \beta_L R$ equal for each term in the interaction potential, i.e. $\beta_{LR} R_R = \beta_{LI} R_I = \beta_{LC} R_C$. These two approaches to the DWBA analysis will henceforth be referred to as β scaling and βR scaling, respectively.

When discussing deformations measured by different experimental techniques, it is more common to compare defor-mation lengths $\delta_L = \beta_L R$. The nuclear matter deformation may then be obtained from the potential deformation through the relation $\beta_{LM} R_M = \beta_{LP} R_P$, where R_M, R_P, β_{LM}, and β_{LP} are the

mass and potential radii and deformation parameters respectively. The choice of R_R, R_I, or R_C as R_p will be discussed in the next section.

Investigations were performed to facilitate a propitious choice for the matching radius and integration step size to be utilized in the distorted wave calculations. These investigations were performed on the elastic as well as the inelastic cross sections. In the latter case, angular distributions were obtained for integration step sizes between .035 and .30 fm, for a matching radius of 14 fm and between .05 and .30 fm for a matching radius of 20 fm. As step size was decreased, the calculated differential cross sections for the two matching radii asymptotically approached the values obtained for a step size of 0.04 fm and .05 fm, respectively. These observations were based on an angular range of 0°-180°. However, it was found that in the angular range of our experiments, 5°-50°, the calculated angular distributions were quite similar for integration step sizes between 0.08 and 0.12 fm. Therefore an integration step size of 0.10 fm was used in subsequent analyses. Using this integration step size, angular distributions were then obtained for matching radii between 15 and 25 fm. When matching radii between 17 and 23 fm were used, the calculated angular distributions were nearly identical. Therefore, in subsequent analyses, we used 20 fm for the matching radius.

2.4 DWBA Results

The optical model parameter sets of Table 2 give the best fits to the elastic scattering of Huffman et al.[5] Results of the searches performed in fitting their data displayed signs of both continuous and discrete ambiguities. Each optical model (OM) set of Table 2 corresponds to the best fit for each of the five "families" of parameters observed. It was anticipated that our inelastic scattering data would remove or reduce the observed ambiguities when compared to DWBA inelastic angular distributions generated using these OM sets.

The theoretical inelastic angular distributions predicted by these five OM sets were very similar over the angular range for which data were obtained. In particular, the only observable differences were slight continuous changes in the depths of the minima with increasing value of the real potential depth V. These changes were most easily observable in the 2^+ states, but did occur to a much lesser extent in the 3^- and 4^+ states. Also, these changes, even for the 2^+ states, were less than the uncertainty in the data.

The above observations hold for both β and βR scaling; the difference between the two types of analyses being that βR scaling gives slightly deeper minima and a slightly steeper overall slope for all states. Also, there is little change in the quality of the fits to the data when switching from one type of analysis to the other for a particular set of OM parameters.

To illustrate the high degree of similarity between the theoretical angular distributions calculated using different OM sets the extremes of these calculations are shown in Figures 3 and 4. Figure 4 shows the V = 60 MeV (solid line) and V = 295 MeV (dashed line) fits to the data when the β—scaling analysis technique is employed. In Figure 3C the V = 160 MeV fits to the data for β scaling (solid line) and βR scaling (dashed line) are shown together. Five of the states are fitted well by the DWBA but the predicted phase of the oscillations does not agree with the observed phase for the other four (viz. the 2.45 MeV (4^+), 2.78 MeV (2^+), 3.90 MeV (2^+), and 4.48 MeV (3^-) states). For the 2.45 MeV (4^+) state, this problem is given more consideration in the next section. Also, small-angle scattering (θ cm $\lesssim$ 15°) is not predicted well for any of the 2^+ states.

Investigations were performed to find which element, if any, of the interaction potential (real, imaginary, Coulomb) was the major contributor to the cross sections. This information could lead to a proper choice of R_R, R_I, or R_C to be used as R_p in calculating the deformation lengths of the potential. Results showed that the imaginary term in the interaction potential gave contributions to the cross sections a factor of approximately three greater than the contributions due to the real term for each of the three angular momentum states observed. Also, Coulomb contributions to the cross sections were important only for the 2^+

Figure 3. Fits to the data for each optical model set using
β scaling (solid line) and βR scaling (dashed
line). Data for which error bars are not shown
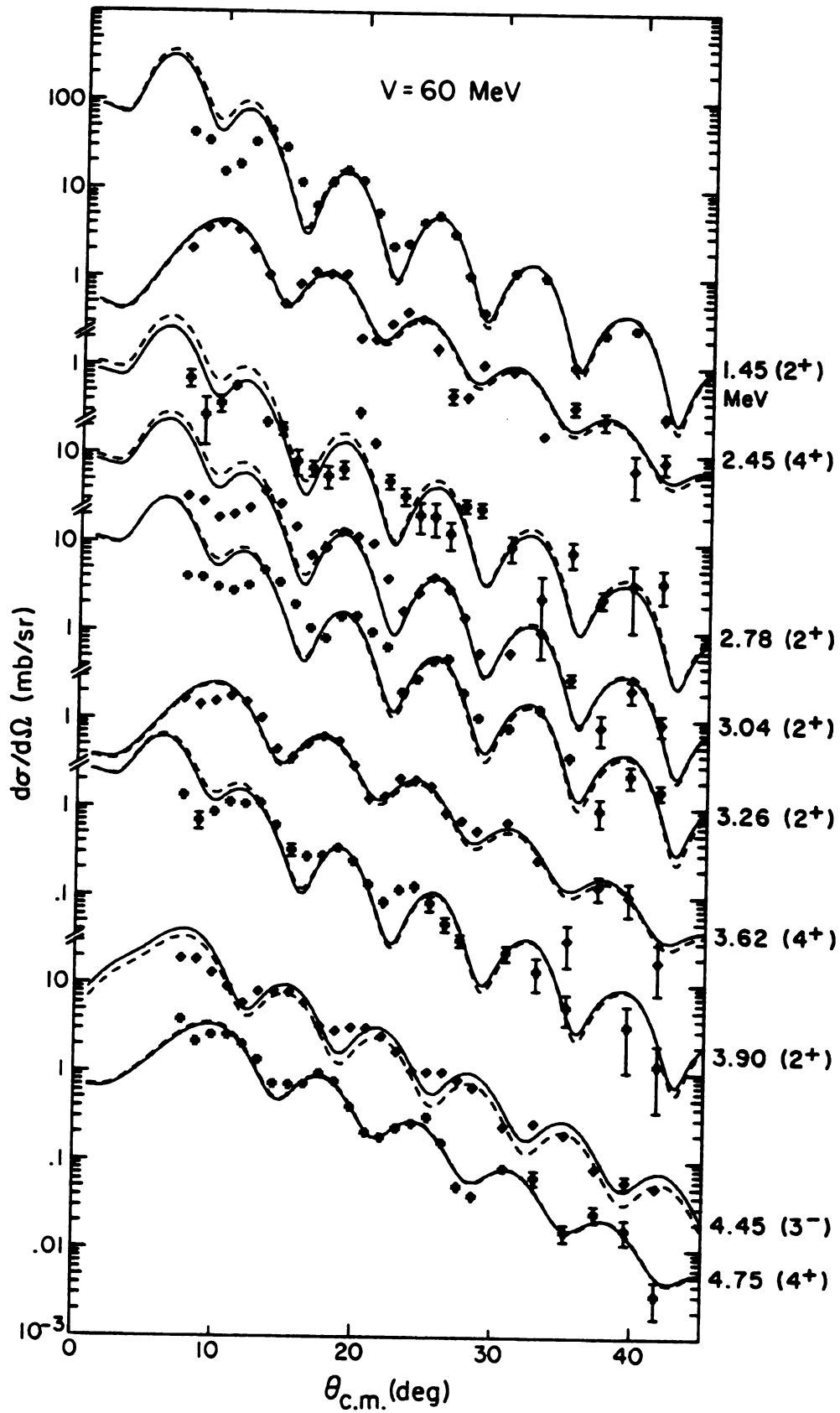have uncertainties less than the size of the
points.

Figure 3A
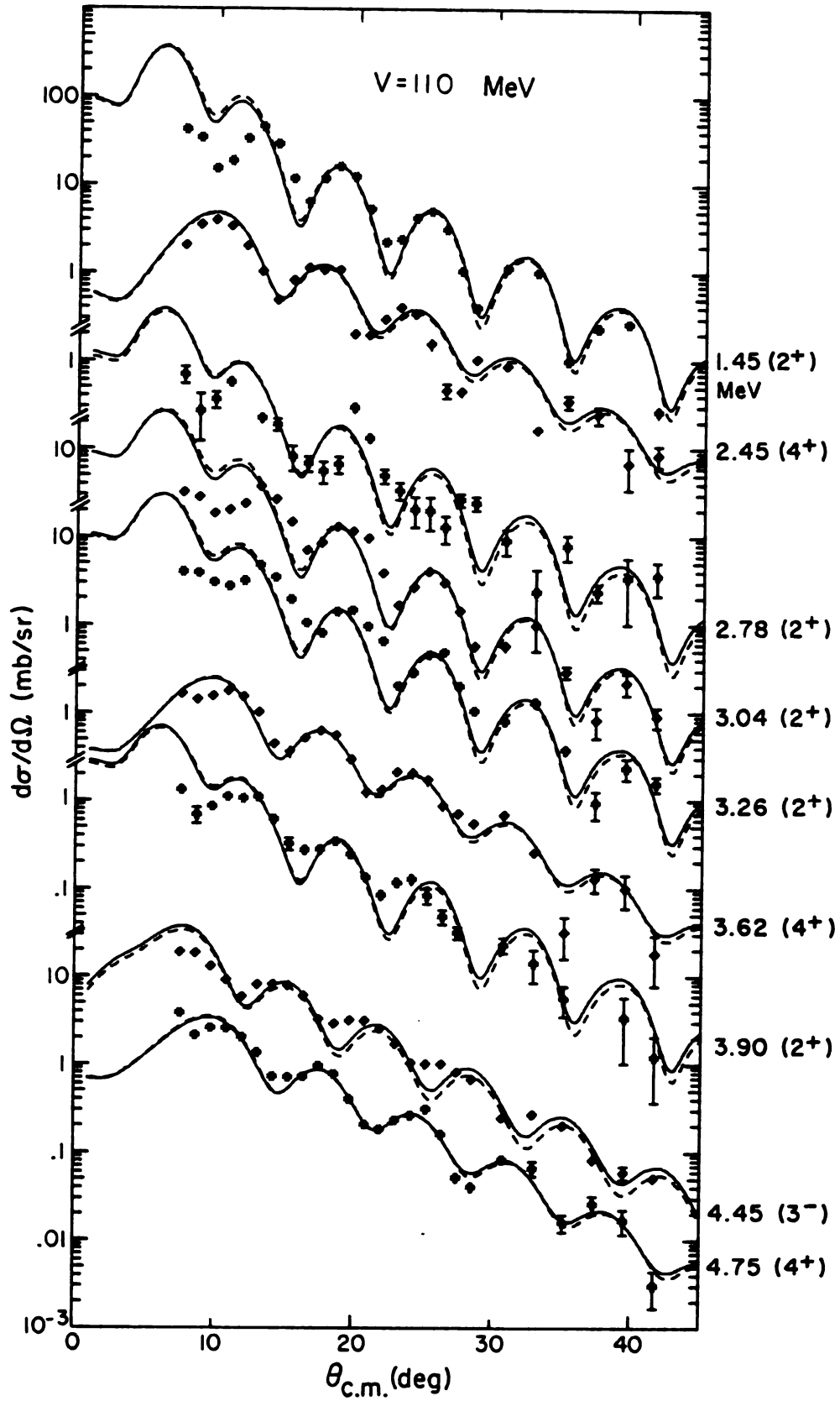
Figure 3B
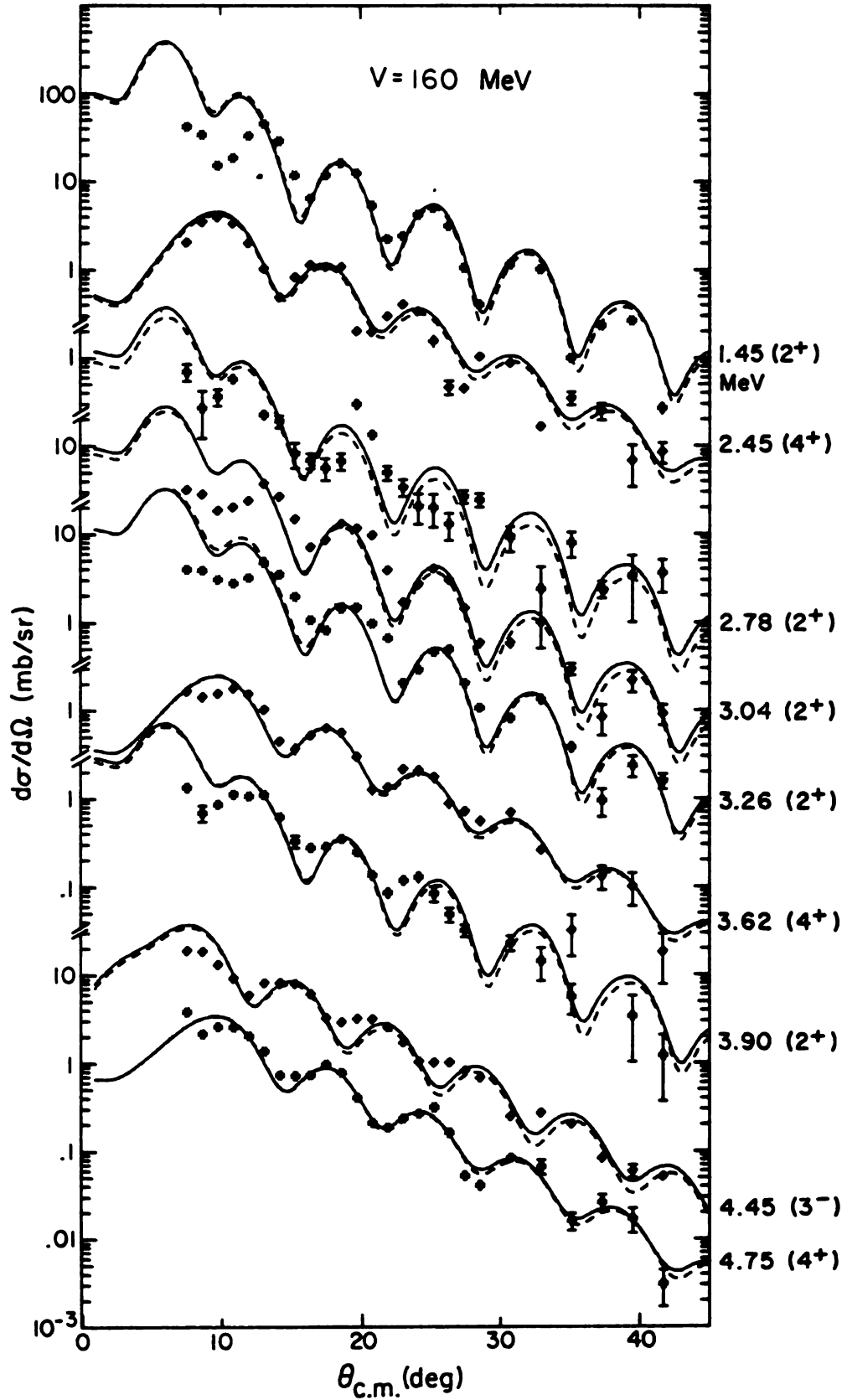
Figure 3C
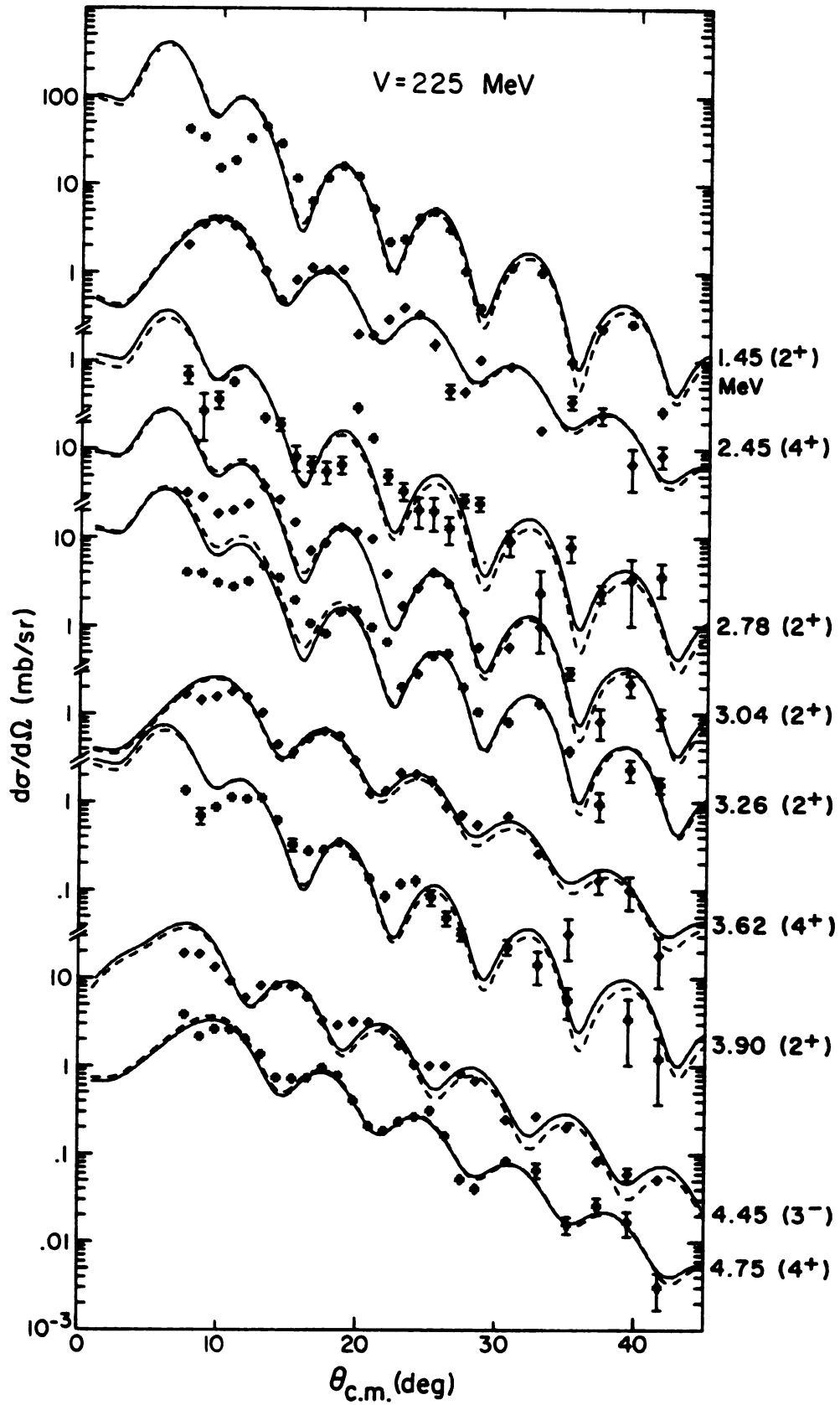
Figure 3D
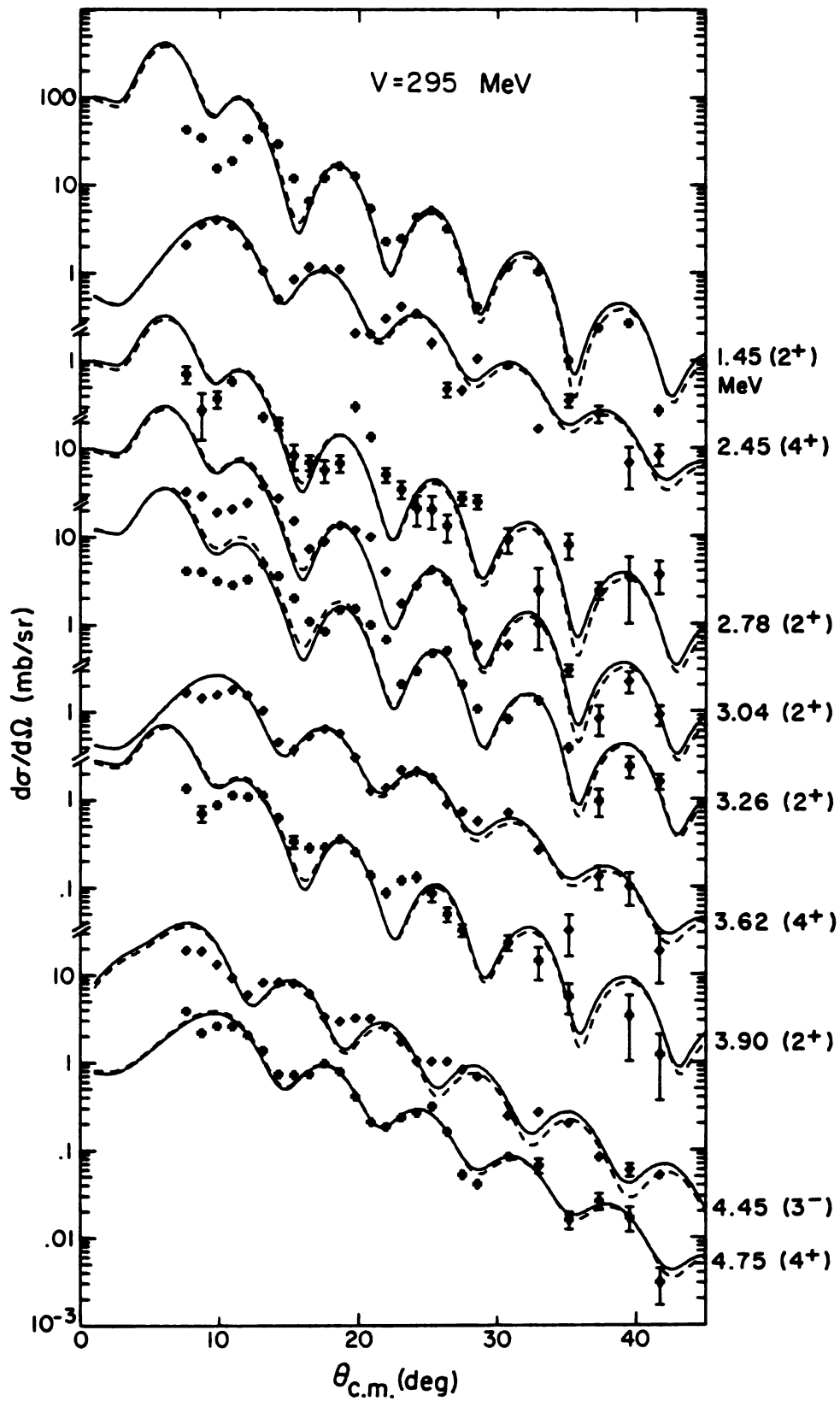
Figure 3E

Figure 4. Fits to data using V = 60 MeV (solid line) and V = 295 MeV (dashed line) optical model sets of Table 2 when using β scaling. Data for which error bars are not shown have uncertainties less than the size of the points.
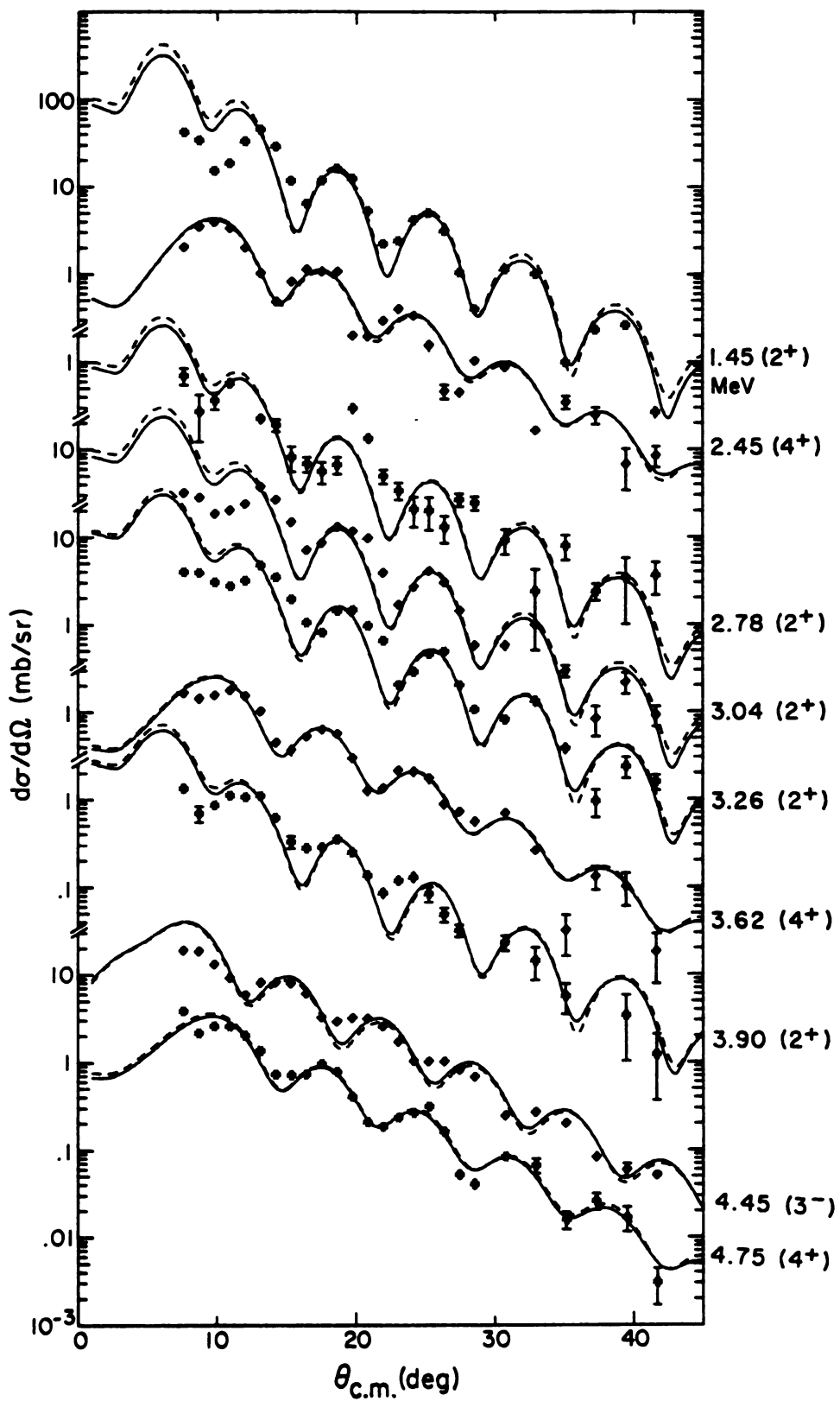
Figure 4

Table 3. Nuclear deformations and deformation lengths of this analysis with deformation lengths of previous analyses. The values reported for this analysis are from the averages of the values obtained independently from the five optical model sets of Table 2. The numbers in parentheses under these values are the standard deviations associated with the averaging processes. Previously reported values include the standard deviations in % and number of observations, respectively, in parentheses under their average. For (p,p'), (α,α'), and other reactions, δ is the average of values reported in references obtained from 20 and in References 17-19. δ_{AV} is the simple average of all references incorporated in the six other columns of previous reported values. Methods of analysis used in extraction of δ_{AV} include DWBA, Austern-Blair diffraction model, coupled channels Born approximation, and measurement of electromagnetic transition strengths.

Table 3.

	β_L Present	βR_I Present	βR Present	δ_{AV} Previous
1.45(2⁺)	0.21 (8)	1.41 (7)	1.17 (1)	.99 (12,43)
2.46(4⁺)	0.054 (4)	.37 (4)	.31 (2)	.51 (14,4)
2.78(2⁺)	0.021 (9)	.14 (9)	.11 (5)	.21
3.04(2⁺)	0.060 (8)	.40 (6)	.34 (2)	.29 (10,3)
3.26(2⁺)	0.066 (7)	.45 (5)	.38 (4)	.35 (12,4)
3.62(4⁺)	0.042 (6)	.28 (5)	.24 (2)	.32 (23,3)
3.90(2⁺)	0.032 (6)	.22 (5)	.18 (1)	.18 (9,2)
4.48(3⁻)	0.12 (5)	.84 (4)	.67 (2)	.80 (17,26)
4.75(4⁺)	0.050 (6)	.34 (5)	.29 (2)	.44 (18,3)

Table 3 (cont'd.).

	δ(p,p')	δ(α,α')	δ others			
1.45(2$^+$)	1.00 (12,12)	.99 (9,10)	(e,e') .90 (13,2)	(d,d') .92 (7,7)	(^{3}He,^{3}He') 1.01 (8,4)	(^{16}O,^{16}O') 1.12 (24,2)
2.46(4$^+$)	.56	.46 (16,2)	Coul. Ex. .87 (12,10)	(n,n') 1.06	(^{18}O,^{18}O') 1.10 (20,2)	
2.78(2$^+$)		.21	(e,e') .57			
3.04(2$^+$)		.28 (13,2)	(e,e') .29			
3.26(2$^+$)		.31 (1,2)	(e,e') .40	(^{16}O,^{16}O') .37		
3.62(4$^+$)	.39	.24 / .33				
3.90(2$^+$)	.19	.17	(^{16}O,^{16}O') 1.00			
4.48(3$^-$)	.83 (12,10)	.80 (23,9)	(d,d') .66 (4,2)	(^{3}He,^{3}He') .76 (14,8)		
4.75(4$^+$)	53	.40 (3,2)				

Figure 5.   Nuclear deformations of this analysis along with
            the ranges and averages of previous analyses. ●
            for βR_I (DWBA, β scaling), ▲ for βR (DWBA, βR
            scaling)$_4$ and ■ for βR_I (coupled channels, first
            2^+ and 4^+ only). See Tables 3 and 4 for related
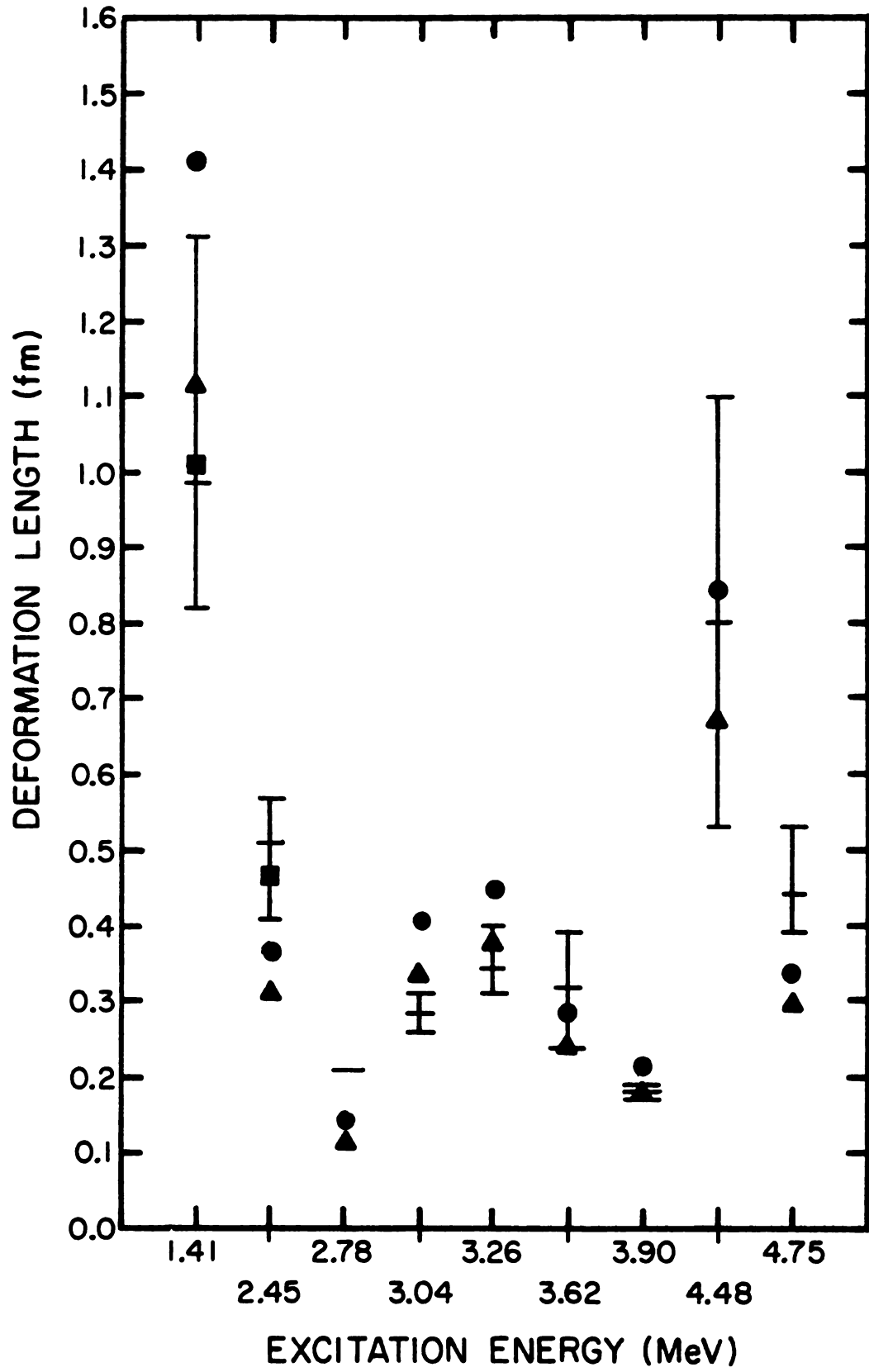   values.

Figure 5

states and then only for angles less than approximately 15°. Thus, R_I was chosen to be R_p and subsequently used to calculate the nuclear deformation lengths of the potential. The imaginary radius has also been used to calculate deformation lengths for other targets at different [6]Li beam energies.[3,4]

In Table 3, values of β, βR_I (from β scaling analysis technique) and βR (from βR scaling) are listed along with the δ values of previous analyses. The values of β, βR, and βR_I listed in Table 3 for this analysis were obtained by averaging the five values independently obtained from each OM set for a given state. The standard deviations associated with these averaging processes are also listed in the table.

From Table 3 we see that the βR_I values are always about 20% greater than the βR values. In comparison to previous determinations of δ, βR_I is closer to δ_{AV} for five of the states and βR is closer for four of the states. Also, βR_I is within the range of previous determinations of δ for only two states, whereas βR is within the recorded range for five states. This is shown more clearly in Figure 5, where high, low, and average values of δ are shown with βR_I and βR.

In addition, the standard deviations associated with the βR_I are larger than those associated with βR by a factor of approximately three. Also noticeable for any given state is a trend in the individual values of βR_I (before averaging) to increase with increasing depth of the real potential when

going from one OM set to another. No such trend was noticed in the βR values.

The βR values differ from the previously reported δ values, most noticeably for the 4^+ states, but the difference is less than with β scaling. βR values for the other states do not agree well with the δ values either, except for the 2^+ states at 3.26 and 3.90 MeV. For the 4^+ states, the βR_I values agree with the δ values better than do the βR values, but the differences are still quite significant. Interestingly, note that βR_I and δ agree best (5% difference) for the 3^- state. Overall, though, the values of βR and βR_I of this analysis do not agree very well with the previously reported values.

Significant also is the fact that the ratios of $\beta_2 R_I / \beta_4 R_I$ ($= 1.67$) and $\beta_2 R / \beta_4 R$ ($= 1.75$) are quite similar and differ from the ratio of δ_2 / δ_4 ($= 1.23$) by about 40%. A similar observation may be made from recent analysis of lithium inelastic scattering from ^{90}Zr.[3] Thus, it would seem inaccurate to scale experimental lithium inelastic cross sections for all observed states by the amount required to obtain agreement with previously reported nuclear deformation lengths for 3^- states.

2.5 Coupled Channels Analysis and Results

Coupled channels calculations were performed using the code ECIS.[13] The optical potential used was that of Table 2

with V = 160 MeV, and the computational parameters were set equal to those used in DWUCK 72: $R_{coul} = 1.40A_2^{1/3}$, 85 partial waves, and integration to a maximum radius of 20 fm in steps of 0.10 fm. The deformation parameters for each portion of the potential were set equal (i.e. $\beta_R = \beta_I = \beta_C$) and the transition matrix elements were calculated internally, in ECIS.

Only the ground state, 1.45 MeV (2^+), and 2.46 MeV (4^+) states were coupled in the present analysis. These states may be effectively coupled in the first-order vibrational model when the 4^+ state is assumed to be an admixture of one- and two-phonon components.[6,7,15] This allows for direct transitions to the 4^+ states, which are not usually included in first order. However, the second-order vibrational model was used because it was believed that reorientation matrix elements would have a sizable effect on the calculated angular distributions. In fact, this effect was subsequently found to be negligible.

Initially, β_2 and β_4 were set to the values obtained from the previous DWUCK 72 analyses. The mixing parameter (BT) describing the mixing of one- and two-phonon components for the 4^+ state was initialized at 18.4° (10% 2 phonon and 90% 1 phonon). Searches were then performed on β_2, β_4, and BT, independently, forcing a simultaneous fit to the 2^+ and 4^+ states. Then a simultaneous search on β_2 and β_4 was performed and finally a simultaneous search on all three was

performed to optimize the fit (minimize χ^2) to the data. These results are given in Table 4. It is seen that the coupling has decreased β_2 and increased β_4.

Results of the coupled-channels calculations are shown in Figure 6. For elastic scattering, the differential cross sections for angles $\lesssim 25^O$ were identical to those predicted by DWUCK 72, and for angles $\gtrsim 25^O$, the differential cross sections were slightly lower and somewhat out of phase. This difficulty might be overcome by using the ECIS code to search on the OM parameters while fitting the elastic and inelastic scattering simultaneously. The fit to the 2^+ data was good except that the amplitude of the oscillations was too small. Therefore, the fit to the data was not quite as good as that predicted by DWUCK 72. The encouraging aspect of this analysis for the 2^+ state is that the small angle data ($\theta cm \lesssim 15^O$) were fitted much better than the DWUCK 72 case.

Finally, the fit to the 4^+ state was vastly improved. The coupled channels analysis reproduced the phase of the data extremely well, and the amplitude of oscillation suggested a very good fit to the data. These were difficulties which the DWUCK 72 analysis could not overcome.

Listed with the final ECIS-related values of β_2, β_4 and BT in Table 4 are the calculated values of βR_I. The final value of BT represents a mixture of 53% 2 phonon and 47% 1 phonon coupling for the 4^+ state. The β_2 value from the coupled channels analysis does not agree with the previously

Table 4. Final values of the nuclear deformations, deforma-
tion lengths, and one- plus two-phonon mixing
parameter, BT, obtained from coupled channels
analysis.

	2^+	4^+
β_L	0.161	0.0686
$\beta_L R$	1.09	0.467
BT		43.75

Figure 6. Comparison of ECIS (solid line) and DWUCK 72
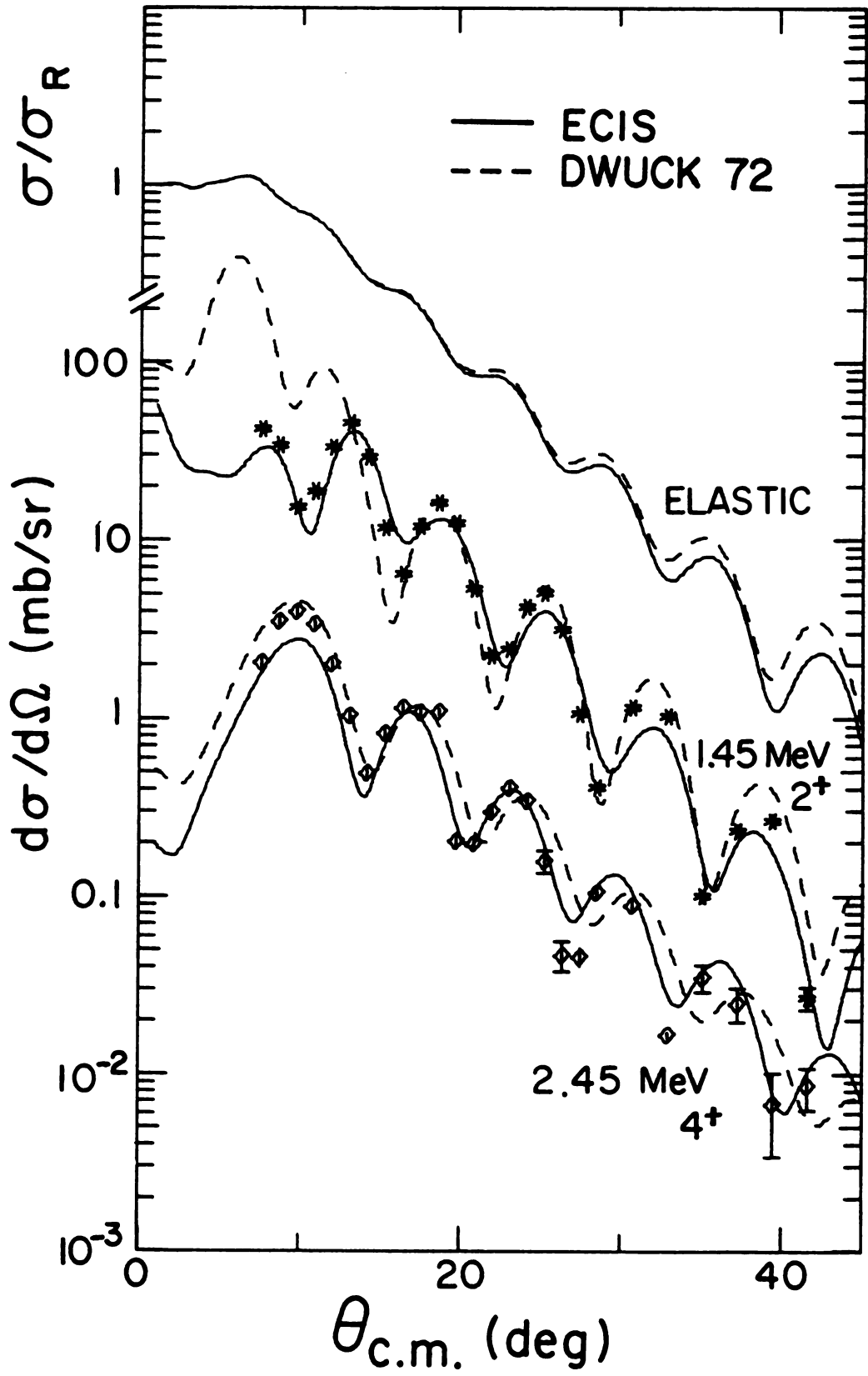(dashed line) for elastic (ratio-to-Rutherford)
and first two excited states.

Figure 6

reported value quite as well as that found with the DWUCK 72 analysis but the β_4 value from ECIS does agree better. Outstanding is the fact that the βR_I values determined here agree with previously reported values much better than does either the β or βR scaling analysis techniques used in DWUCK 72. Also, both βR_I values are within the range of previous values.

Results of the present work confirm the observation of Buck[6] and of Horen et al.[7] that the 4^+ state at 2.45 MeV is an admixture of one- and two-phonon transitions. Buck investigated only the effects of multiple-plus-direct transitions and obtained good agreement with his 40-MeV alpha-scattering data when the direct two-phonon transition was enhanced by a factor of 1.5 over theoretical predictions. With the diffraction model of Austern and Blair, Horen et al. were unable to simultaneously fit the magnitude and slope of their alpha-scattering data at any of their experimental energies. However, they were able to reproduce the phase of the oscillations of their data. Coupled-channels calculations of the present work reproduced the magnitude, slope, and phase of our ^{6}Li data. Also, coupled-channels effects for the remaining 4^+ states of this analysis at 3.62 and 4.75 MeV appear to be much smaller because DWBA analyses reproduce these distributions well.

2.6 Conclusions

No resolution or reduction of the OM ambiguities was possible through this DWBA analysis. Each of the five OM sets used to describe the interaction gave virtually identical fits to the elastic data over the angular range for which data were obtained and gave very similar fits to the inelastic data. It is believed[16,22] that more backward angle data for the elastic scattering could remove the observed ambiguities.

Coupled-channels calculations were performed only as a preliminary study to explore their possible effect on inelastic states poorly fitted by the DWBA. It was found that these coupled-channels calculations were able to more accurately predict the phase of the oscillations for the 2.46 MeV (4^+) state but only at the expense of reduced quality in the fit to the 1.45 MeV (2^+) inelastic scattering. Finally, the deformation lengths obtained with the β values extracted from the coupled-channels calculations agreed with previously reported values better than did those produced by the DWUCK 72 calculations.

APPENDICES

APPENDIX A

Elastic Scattering

Elastic scattering data were gathered using the 40"
scattering chamber at the Michigan State University Cyclotron
Laboratory. Cyclotron, source, and beam parameters were the
same as those for the inelastic scattering experiment except
that a beam energy of 73.4 MeV was employed. Initially, a
movable ΔE–E detector pair was used along with a monitor fixed
at 20°. In order to reduce energy dispersion with this
arrangement, the target was rotated with respect to the beam
by an angle half as large as the detector angle. Periodic
checks on the position of the beam axis relative to the
scattering chamber were performed by measuring the count rate
at equal angles on opposite sides of the beam. This system was
awkward because of the changes in effective target thickness
with angle, and because the checks on the beam axis consumed a
portion of the small (approximately three hour) source
lifetime.

Subsequently a new detector system was used with two ΔE–E
detector pairs situated at opposite but equal scattering
angles. Thus, the target was kept at right angles to the beam
at all times. Also, the orientation of the beam axis was

41

constantly monitored by observing spectra from each detector as they were gathered through the use of a PDP 11/45 on-line computer. Most importantly, this doubled the effective count rate at each angle and provided a more efficient usage of the beam time. All data presented in this study were gathered using this latter technique. A block diagram of the apparatus is presented in Figure A1 and a typical spectrum is presented in Figure A2. Accuracy of the data, unless otherwise specified, is ± 4% relative with an additional ± 5% absolute. The data are presented in Table A1.

Analysis of the data was performed using an optical potential with volume real and volume imaginary terms of the Woods-Saxon form with a different geometry for each term:

$$U(r) = -Vf(r) - iWg(r)$$

where $f(r) = [1 + \exp(\frac{r-R_R}{a_R})]^{-1}$,

$$g(r) = [1 + \exp(\frac{r-R_I}{a_I})]^{-1}$$

and $R_R = r_R A^{1/3}$, $R_I = R_I A^{1/3}$.

Added to this was the Coulomb potential due to a spherically symmetric charge distribution of radius $R_c = 1.40 A^{1/3}$ fm.

Calculations of the theoretical angular distributions and searches on the parameters of the optical potential were performed on an XDS Sigma-7 computer using the code SGIBELUMP.[23] As for the inelastic scattering, a study of the matching
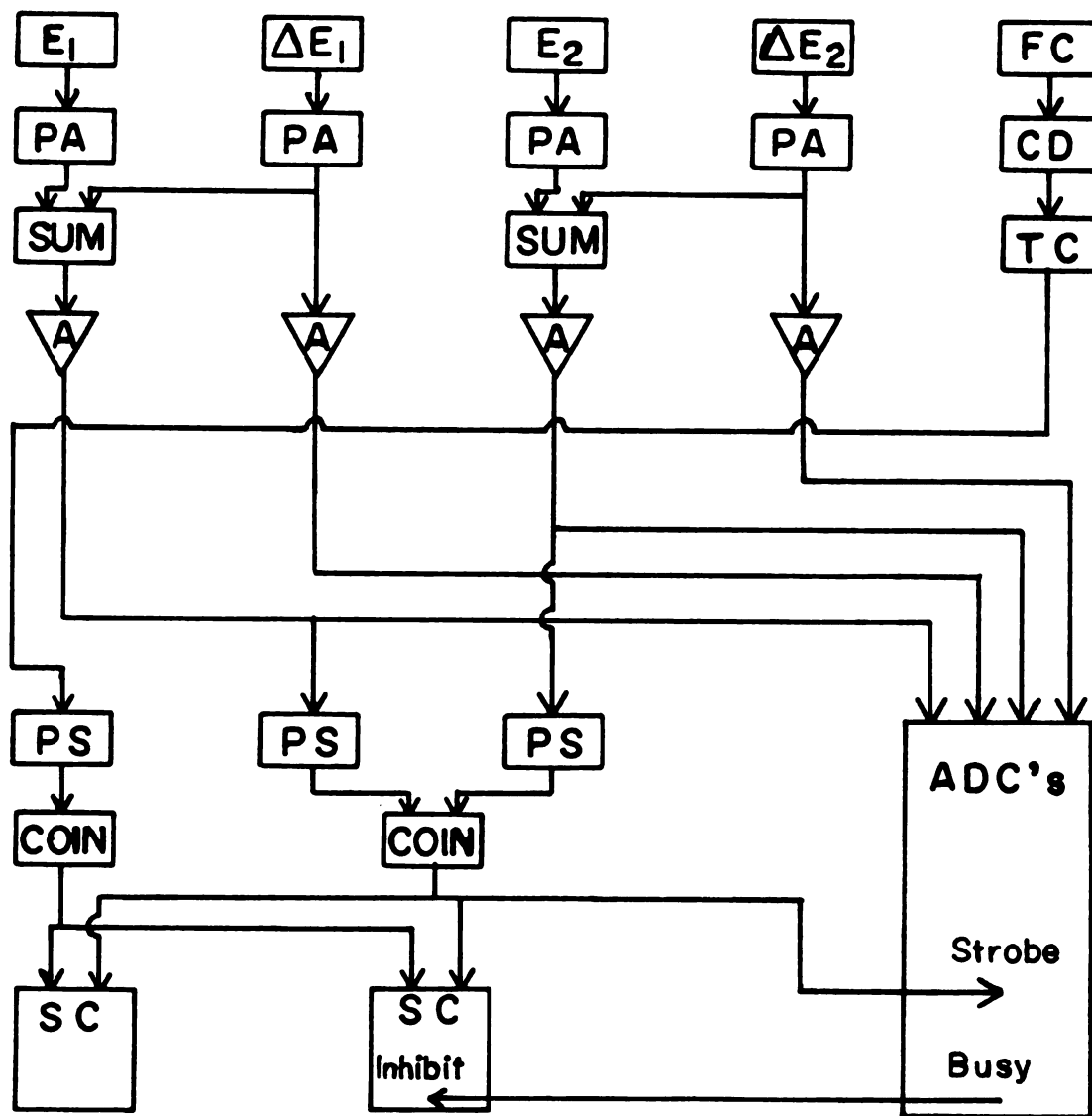
Figure A1. Block diagram of apparatus for the elastic scattering experiment. For explanation of abbreviations, see Figure 1.
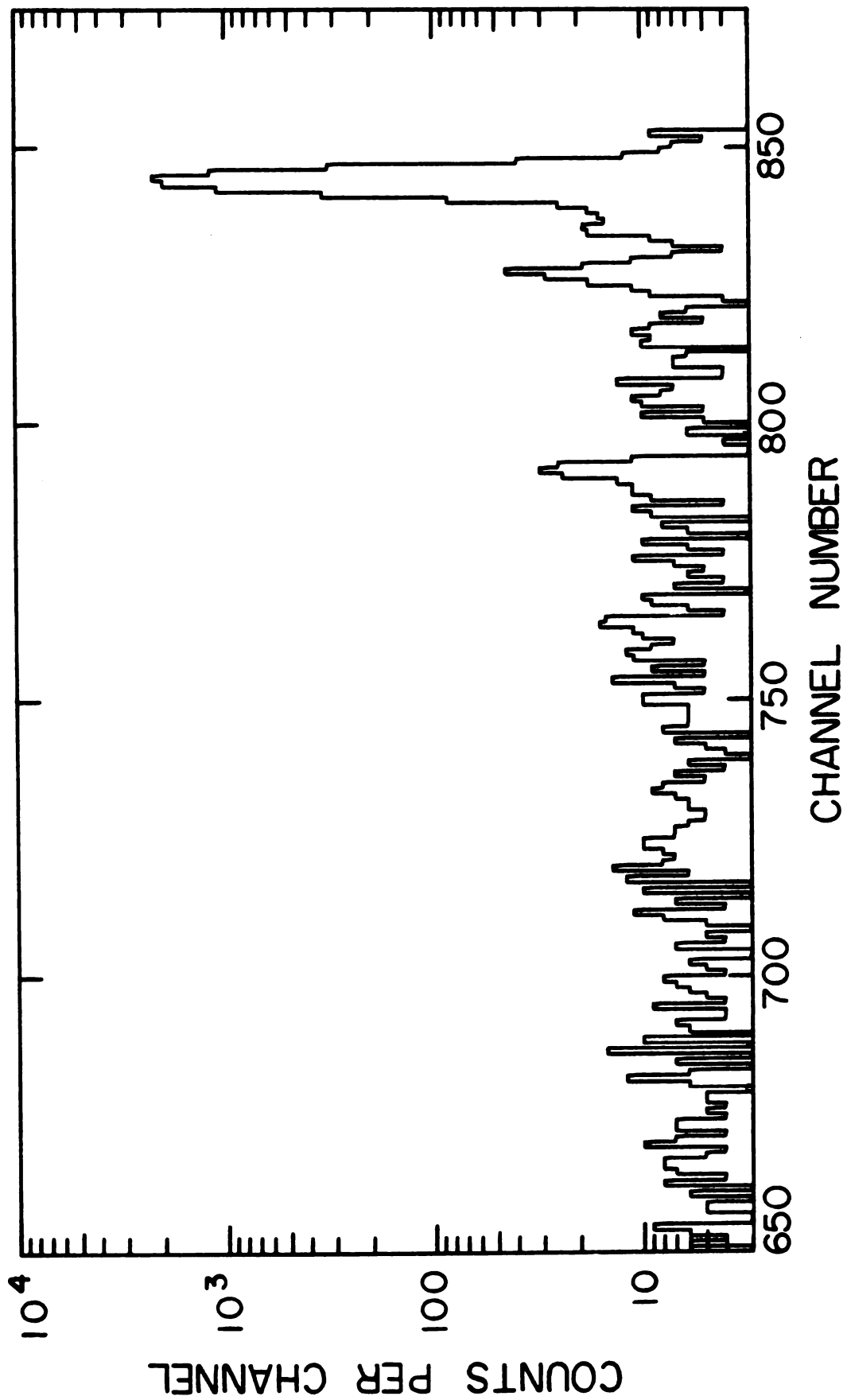
Figure A2. Typical spectrum for the elastic scattering experiment.

Table A1. Elastic scattering data from the 73.4 MeV experi-
ment. The cross sections are in mb/sr.

| θ_{cm}	$d\sigma/d\Omega$	$\Delta\sigma(\%)$
7.72	8.8345E 04	4.8
8.83	4.0541E 04	3.1
9.93	2.4063E 04	3.1
11.03	1.3876E 04	3.1
12.14	7.2315E 03	2.3
13.24	3.6450E 03	2.4
14.34	2.2258E 03	2.3
15.44	1.5592E 03	2.2
16.54	1.0452E 03	2.3
17.64	5.8204E 02	2.5
18.74	3.0116E 02	2.8
19.84	1.9894E 02	2.6
20.94	1.6833E 02	2.7
22.03	1.3349E 02	2.7
23.13	7.8028E 01	3.2
24.23	4.3816E 01	3.2
25.32	2.3223E 01	3.5
26.42	2.0316E 01	3.3
27.51	1.9577E 01	3.2
28.61	1.5425E 01	3.5
29.70	9.5966E 00	3.4
30.79	4.4327E 00	3.5
31.89	2.4079E 00	3.9
32.98	2.5453E 00	2.6
34.07	2.7607E 00	3.1
35.15	2.3302E 00	3.3
36.24	1.4686E 00	3.7
37.33	5.4995E-01	3.8
38.41	2.7611E-01	4.5
40.58	4.4980E-01	5.0
42.75	2.6266E-01	6.6
43.83	1.2997E-01	6.4
44.91	3.0614E-02	7.9
45.98	2 6631E-02	6.6
48.14	5.4517E-02	8.2
50.28	2.9815E-02	8.8
52.43	4.7907E-03	30.0
54.56	1.1359E-02	11.0
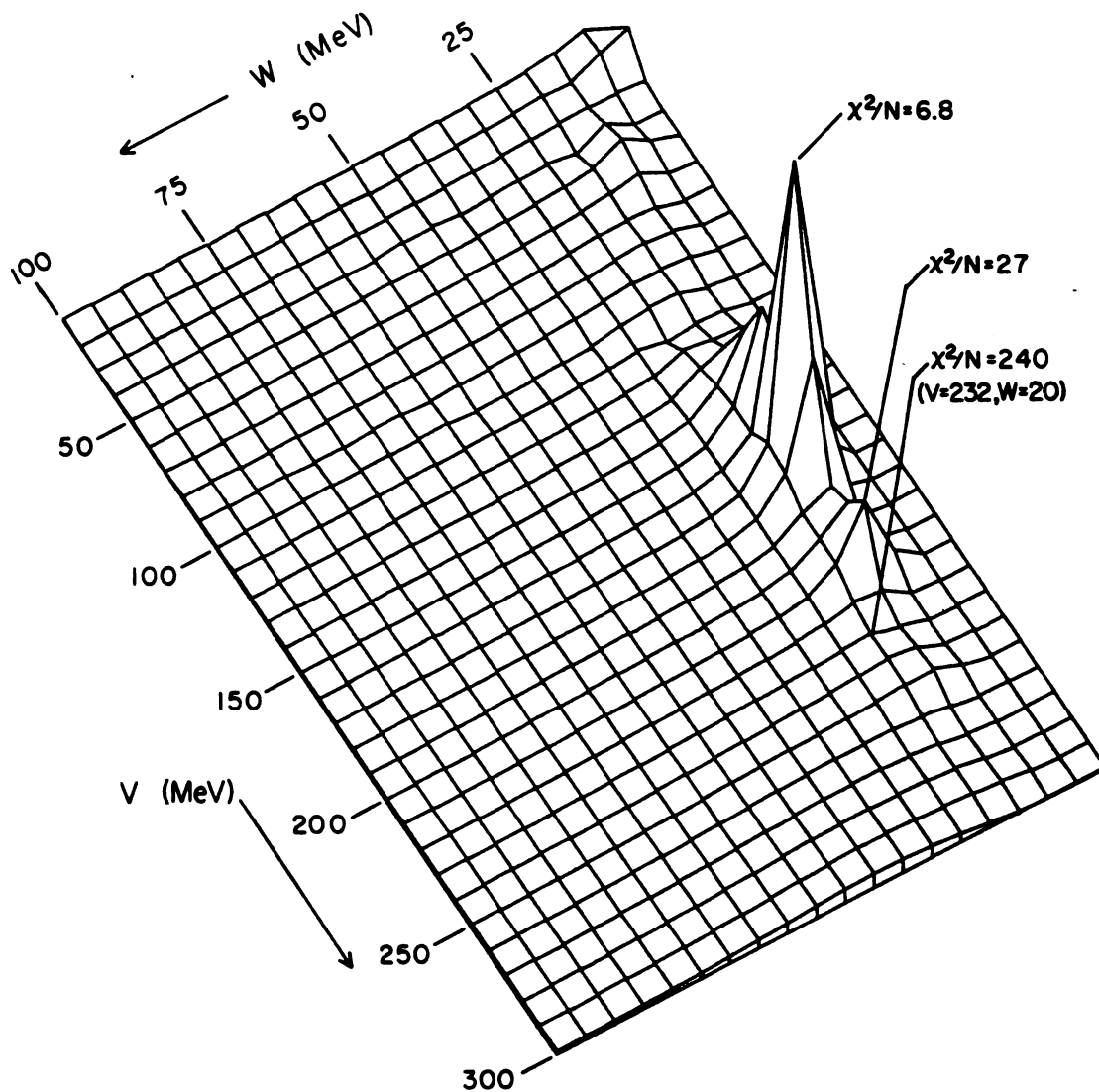
Figure A3. Three dimensional plot of χ^2 vs. V and W for a grid on V and W using the geometry parameters of Chua et al.[1] (viz. V = 232 MeV, r_R = 1.3 fm, a_R = .70 fm, W = 20 MeV, r_I = 1.7 fm, a_I = .90 fm).

radius and integration step size was performed to find values
of these parameters for which the theoretical angular distri-
butions were approximately constant. First, matching radii
between 10 and 25 fm were examined with a resulting choice of
17 fm for future calculations. Using this value, the
integration step size was then varied between 0.05 and
0.15 fm with a resulting choice of 0.10 fm for future
calculations.

To become familiar with the optical model (OM) parameter
space which could fit the elastic scattering data, a grid
over V and W was completed using fixed geometry parameters
from the 50.6 MeV elastic study of Chua et al.[1] The criteria
for a good fit was a minimum in the value of χ^2:

$$\chi^2 = \sum_{i=1}^{N} \{[\sigma_{ex}(\theta_i) - \sigma_{TH}(\theta_i)]/\Delta\sigma_{ex}(\theta_i)\}^2$$

where N is the number of data points. In a three dimensional
plot of χ^2 versus V and W, it was very difficult to see the
minima due to their extreme depth compared to the surrounding
area of high χ^2 values. Therefore a suitably scaled plot of
$1/\chi^2$ versus V and W was deemed the most appropriate for lucid
visualization of the results. This plot is given in
Figure A3. The "zero" level of the z—axis in Figure A3
corresponds to a χ^2 per point (χ^2/N) of 26×10^5 and the
pinnacle of the highest peak corresponds to a χ^2/N of 6.8. It
is seen from the plot that the best fits to the data occur for
values of V between 130 and 220 MeV, and for values of the W
around 20 MeV. These results are borne out by the best fit OM

sets presented in Table 2. In fact, the peak which represents the deepest minimum in χ^2 (V = 170, W = 20 MeV) corresponds closely with V and W for one of the best fit parameter sets of Table 2. Also evident from Figure A3 is an indication of the energy dependence of V and W for the ^{6}Li + ^{58}Ni reaction. The best fit values of V = 232 and W = 20 MeV for E = 50.6 MeV are found to shift to V = 170 and W = 20 MeV for 73.4 MeV scattering when the geometries are held fixed.

To find the OM sets which produced the best fits to the data, SGIBELUMP was used in a search mode which minimized χ^2. Three distinct sets of preliminary searches were performed using the 50.6 MeV parameters of Chua et al.[1] as a starting point. For each set of searches, a grid was performed on the real well depth V between 10 and 300 MeV in 10 MeV increments. In the first set of searches, the OM parameters were varied in pairs (r_R, r_I; r_R, W; a_R, a_I; a_R, W) followed by a combination varying W, r_I, a_I as a group and finally varying r_R, a_R, W, r_I, a_I as a group. This sequence was initially completed for the V = 160 MeV data point, the results of which were then used as starting parameters in the V = 150 and 170 MeV search sequences. The results of the V = 150 MeV search sequence were then used as starting parameters for the V = 140 MeV grid point. This algorithm was continued down to V = 10 MeV and similarly from V = 160 MeV up to 300 MeV.

The second set of searches employed the same search sequence as the first set, the difference between the two sets of searches being that in the second set the 50.6 MeV parameters were used as starting parameters for each grid point. The values of the OM geometry parameters were slightly different between the two sets of searches with a noticeable difference between the values found for the imaginary well depth W. For V = 200 MeV the difference was most notable in that the second set of searches gave values of W approximately 50-60% lower than the first set of searches. Values of χ^2 were comparable.

The third set of searches was the most lengthy. The 50.6 MeV parameters (except r_R) were used as starting parameters for each grid point. The value of r_R was held fixed during the majority of this set of searches at 1.26 fm in an attempt to avoid the Vr_R^n ambiguity. This value of r_R is the average obtained in the second search sequence. The remaining OM parameters were searched upon in pairs (a_R, r_I; a_R, W; a_R, a_I) followed by a simultaneous search on W, r_I, a_I as a group. The OM parameters which gave the best fit to the data from this search sequence were then used in the same search sequence for each data point. The results of this second run-through of the sequence were then used as starting parameters for a search on r_R followed by a simultaneous search on r_R, a_R, W, r_I, a_I for each data point.

Finally, the results of all three sets of searches were examined and combined to form a composite grid representing the best fits to the data. The OM parameter sets for each grid point were used as starting parameters for a search on V followed by a search on all six OM parameters. Most of the grid points remained approximately constant in χ^2 and retained OM parameters very near their starting values. However, there were five distinct areas in which χ^2 was considerably reduced. For each of these minima, a five parameter search was then performed while holding V fixed for grid values in steps of five MeV for a total of 30 MeV in each direction from the minima. Starting parameters for each of these grid points were the OM parameters (except V) for the nearest value of V representing one of the five minima in χ^2. It should be noted that in all of the above searches, the uncertainty for the data point at $\theta_{cm} = 52.4^{\circ}$ was artifically increased from 18% to 30%.

The results of all the searches performed are shown in Figure A4. From the plot of χ^2/N versus V, we observe the familiar continuous and discrete ambiguities. The values of the OM parameters for the five minima in χ^2 are given in Table 2 and their respective fits to the data are displayed in Figure A5. From the plots of Figure A5, we see that there is no possible resolution of the OM ambiguities represented in Figure A4 over the limited angular range for which data were gathered. It was anticipated that comparison of the

Figure A4. Results of searches on optical model parameters
performed in fitting the elastic scattering data.
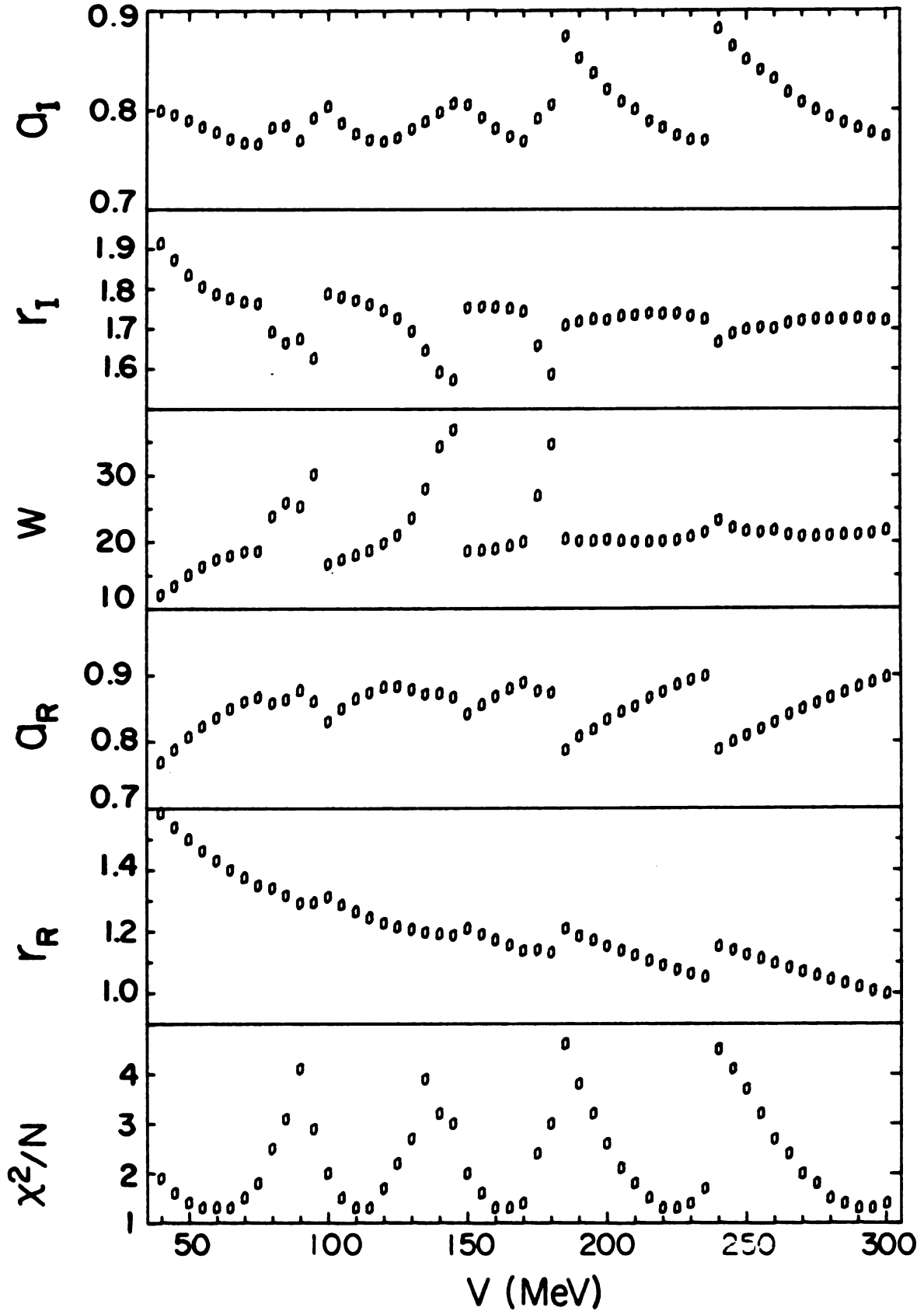
Figure A4
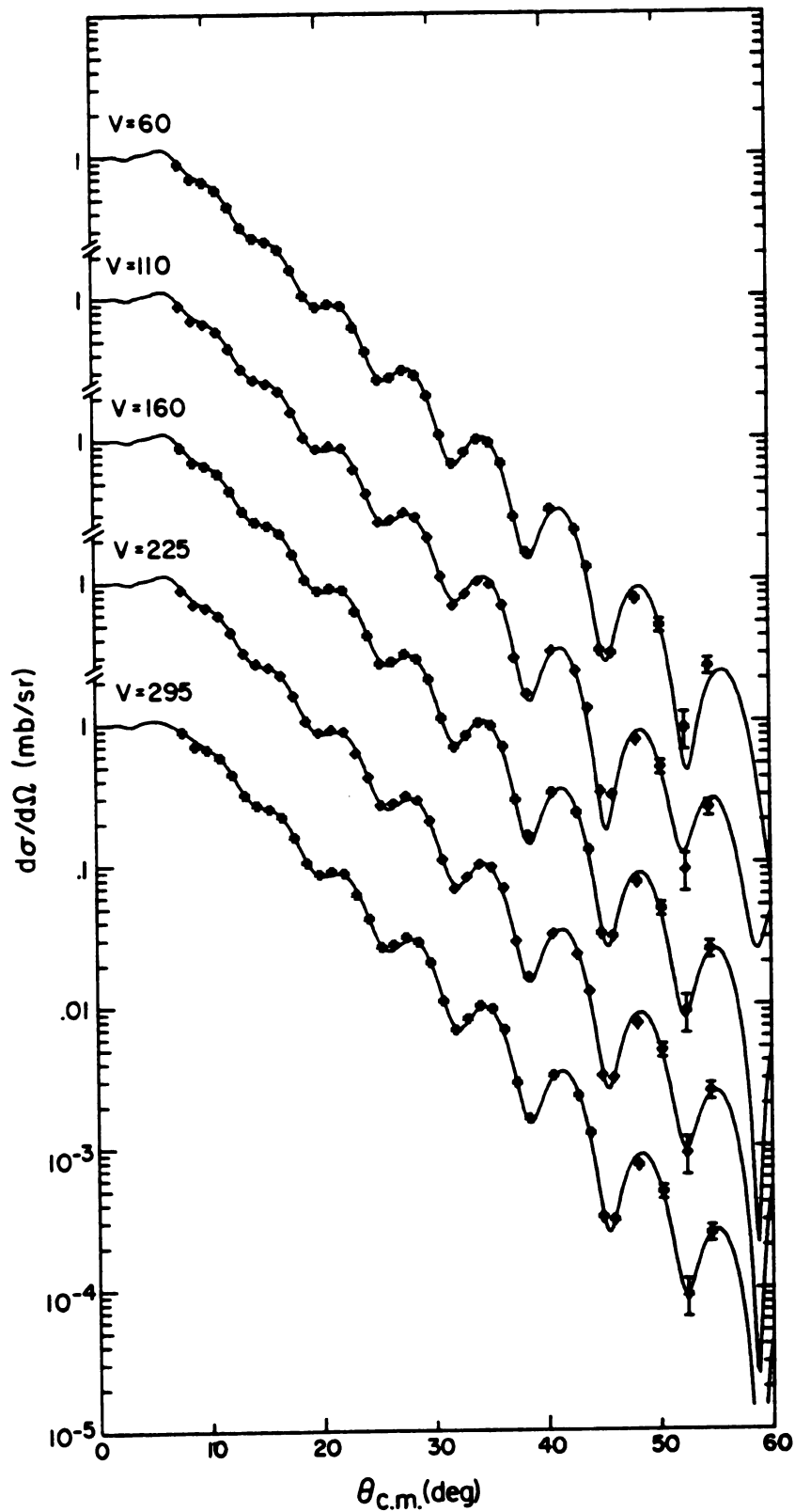
Figure A5. Fits to the elastic scattering data provided by each of the five sets of best fit optical model parameters of Table 2.

experimental inelastic angular distributions with those pre-
dicted by the above OM sets would remove or reduce the OM
ambiguities. This was found not to be the case and it is
believed[16,22] that the OM ambiguities may be resolved by
obtaining elastic scattering data at more backward angles
and/or higher energies.

APPENDIX B

The Theory of Inelastic Scattering
via Direct Transitions

B.1 The Distorted Wave Born Approximation

Consider the Hamiltonian:

$$H = \frac{-\hbar^2}{2\mu} \nabla^2 + U(r) + H_\xi - V(\vec{r}_f, \xi) \tag{1}$$

where r represents the position of the projectile and ξ represents the internal degrees of freedom of the target nucleus. The optical potential is U and H_ξ is the Hamiltonian which describes the internal motion of the target. The kinetic energy is expressed in terms of the reduced mass of the system and V is the interaction potential involving the final state channel f. This total Hamiltonian has solutions Ψ to the Schroedinger Equation

$$H\Psi = E\Psi \tag{2}$$

Also, for the target Hamiltonian H_ξ, we have

$$H_\xi v_\nu(\xi) = \epsilon v_\nu(\xi) \tag{3}$$

where the subscript ν on the solutions may refer to either

the initial state i or the final state f. In the asymptotic region, the solution to (2) looks like

$$\psi^{(+)} \rightarrow v_i(\xi) e^{i\vec{k}_i \cdot \vec{r}_i} - \sum_f A_f v_f(\xi) \frac{e^{ik_f r_f}}{r_f} \tag{4}$$

where k_i and k_f refer to the relative momenta of the system in its initial and final states respectively.

The differential scattering cross section for inelastic scattering may be derived[24,25] from (2) and is given by

$$\frac{d\sigma}{d\Omega} = \left(\frac{\mu}{2\pi\hbar^2}\right)^2 \frac{k_f}{k_i} \sum_{Av} |T_{fi}|^2 \tag{5}$$

where the T_{fi} are amplitudes of the scattering matrix and $\sum_{Av}$ indicates a sum over final spin states and an average over initial spin states. Specifically, T_{fi} is given by

$$T_{fi} = \langle v_f(\xi)\chi_f^{(-)}(\vec{k}_f, \vec{r}_f)|V(\vec{r}_f, \xi)|\psi^{(+)}\rangle \tag{6}$$

This is an exact solution. The distorted waves $\chi_f^{(-)}$ in (6) describe the elastic scattering of the projectile as prescribed by

$$[\nabla_f^2 - \frac{2\mu}{\hbar^2} U(r_f) + k_f^2]\chi_f^{(-)} = 0 \tag{7}$$

If we knew the solution $\psi^{(+)}$ to (2), we would be able to calculate T_{fi} exactly. However, this is not the case and we must therefore make an ansatz of the scattered wave function that will produce a good approximation of the transition matrix.

A standard method is to assume the distorted wave Born approximation, for which $\psi^{(+)}$ is approximated by

$$\psi^{(+)} = v_i(\xi)\chi_i^{(+)}(\vec{k}_i,\vec{r}_i) \tag{8}$$

The transition matrix thus becomes

$$T_{fi} \simeq <v_f(\xi)\chi_f^{(-)}(\vec{k}_f,\vec{r}_f)|V(\vec{r}_f,\xi)|v_i(\xi)\chi_i^{(+)}(\vec{k}_i,\vec{r}_i)> \tag{9}$$

Assuming that the wave functions do not change appreciably over distances on the order of ranges of the nuclear potentials which make up V, we may make the zero range approximation: $r_f = r_i = r$. The transition matrix thus becomes

$$T_{fi} = \int d^3r \; \chi_f^{(-)}(\vec{k}_f,\vec{r})<v_f(\xi)|V(\vec{r},\xi)|v_i(\xi)>\chi_i^{(+)}(\vec{k}_i,\vec{r}) \tag{10}$$

We may now go about finding the matrix elements of the interaction $<v_f|V|v_i>$. Expanded into multipoles, V becomes:

$$V(\vec{r},\xi) = \sum_{\ell,m} V_{\ell m}[i^\ell Y_\ell^m(\hat{r})]^* \tag{11}$$

where the $V_{\ell m}$ must behave under rotations of coordinates like the spherical harmonics $Y_\ell^m(\hat{\xi})$, and have parity $(-)^\ell$. The factor i^ℓ is included to insure the reality of the nuclear reduced matrix elements. Also, we must now make formal use of the spins J and projections M_j of the initial and final state. Employing (11) in (10) and making use of the Wigner-Eckart theorem, we find:

$$<v_f|V|v_i> = <J_f M_f|V|J_i M_i>$$

$$= \sum_{\ell,m}<J_f M|\; J_i \ell M_i m><J_f||V_{\ell m}||J_i>[i^\ell Y_\ell^m(\hat{r})]^* \tag{12}$$

The reduced matrix element is now a function of radius only and is usually referred to as the product of a strength A_ℓ and a form factor F_ℓ:

$$A_\ell F_\ell (r) = \langle J_f || V_{\ell m} || J_i \rangle \ . \tag{13}$$

Then T_{fi} becomes:

$$T_{fi} = \sum_{\ell m} \langle J_f M_f | J_i \ell M_i m \rangle \ B_{\ell m} \ , \tag{14}$$

where

$$B_{\ell m} \equiv \int d^3 r \ \chi_i^{(-)*} (\vec{k}_i, \vec{r}) A_\ell F_\ell (r) [i^\ell Y_\ell^m (\hat{r})]^* \chi_f^{(+)} (\vec{k}_f, \vec{r}) \tag{15}$$

Summing over final and averaging over initial spin states in T_{fi} gives a term of $(2J_f + 1)/(2J_i + 1)(2\ell + 1)$, so the differential cross section (5) becomes:

$$\frac{d\sigma}{d\Omega} = (\frac{\mu}{2\pi\hbar^2})^2 \frac{k_f}{k_i} (\frac{2J_f+1)}{2J_i+1)} \sum_{\ell,m} \frac{|B_{\ell m}|^2}{(2\ell+1)} \tag{16}$$

B.2 Calculation of Form Factors

All that now remains in order to get an accurate expression of the differential cross section is to calculate the form factor. In the collective model used, the rotational and vibrational model form factors are equivalent to first order in the deformations. Therefore only the derivation of the rotational model form factor is herein presented for even-even nuclei.

It is reasonable to assume that the total optical potential strength depends only on the distance of the projectile from the nuclear surface

$$U_{op} \equiv U[r - R(\Theta', \Phi')] \tag{17}$$

where R is a nonspherical surface with body fixed coordinates Θ', Φ' and is usually given by:

$$R(\Theta', \Phi') = R_o[1 + \sum_{kq} \alpha_{kq} Y_k^q (\Theta', \Phi')] . \tag{18}$$

The strengths α_{kq} for a quadrupole deformation, $k = 2$, are related to the familiar deformation parameter β and asymmetry parameter γ by

$$\alpha_{20} = \beta \cos \gamma; \quad \alpha_{2\pm 1} = 0; \quad \alpha_{2\pm 2} = \beta \sin \gamma / 2 \tag{19}$$

Assuming axially symmetric nuclei requires $q = 0$, $\gamma = 0$ and (18) becomes:

$$R(\Theta', 0) = R_o[1 + \sum_{\ell} \beta_{\ell} Y_{\ell}^o (\Theta', 0)] \tag{20}$$

A Taylor-series expansion of the total optical potential about $R = R_o$ yields:

$$U_{op}(r - R_o) = U(r - R_o) - \delta R \frac{\partial U(r - R_o)}{\partial r} + \frac{1}{2} \delta R^2 \frac{\partial^2 U(r - R_o)}{\partial r^2} + .. \tag{21}$$

where

$$\delta R = (R - R_o) = R_o \sum_{\ell} \beta_{\ell} Y_{\ell}^o (\Theta', 0) \tag{22}$$

The first term of the expansion (21) is identified with the spherical optical potential used to describe elastic scattering. The other terms are identified with inelastic scattering. Assuming the term of order β_{ℓ} to be the major contributor to the inelastic scattering, the interaction potential (11) becomes

$$V = \sum_{\ell} i^{\ell} R_o \beta_{\ell} \frac{dU}{dr} Y_{\ell}^{O} (\Theta',0) \ . \tag{23}$$

Converting to space-fixed coordinates via the spherical harmonic addition theorem,

$$Y_{\ell}^{O} (\Theta',0) = \sqrt{\frac{4\pi}{2\ell+1}} \sum_{m=-\ell}^{\ell} Y_{\ell}^{m*} (\hat{r}) Y_{\ell}^{m} (\hat{\xi}) \ , \tag{24}$$

(where $\hat{\xi}$ are the polar angles of the nuclear symmetry axis) yields

$$V = \sum_{\ell,m} i^{\ell} R_o \beta_{\ell} \frac{dU}{dr} \sqrt{\frac{4\pi}{2\ell+1}} Y_{\ell}^{m*} (\hat{r}) Y_{\ell}^{m} (\hat{\xi}) \ . \tag{25}$$

Comparing (25) with (11), we see that the $V_{\ell m}$ values are given by

$$V_{\ell m} = i^{\ell} R_o \beta_{\ell} \frac{dU}{dr} \frac{4\pi}{\sqrt{2\ell+1}} Y_{\ell}^{m} (\hat{\xi}) \tag{26}$$

Using separation of coordinates for the initial and final wave functions, we can say

$$v_i (\xi) = Y_O^O (\hat{\xi}) \cdot \phi$$

$$v_f (\xi) = Y_{J_f}^{M_f} (\hat{\xi}) \cdot \phi \tag{27}$$

For rotational excitation, the radial components ϕ of the nucleus remain constant and therefore do not contribute to the form factor. Thus, using (26) and (27), the reduced matrix element of the potential becomes:

$$A_{\ell} F_{\ell} (r) = i^{\ell} \sqrt{\frac{4\pi}{2\ell+1}} R_o \beta_{\ell} \frac{dU}{dr} \int Y_{J_f}^{M_f*} (\hat{\xi}) Y_{\ell}^{m} (\hat{\xi}) Y_O^O (\hat{\xi}) d\xi \ .$$

Or,

$$A_{\ell} F_{\ell} (r) = i^{\ell} (2\ell+1)^{-1/2} \beta_{\ell} R_o \frac{dU}{dr} \delta_{J_f \ell} \delta_{M_f m} \ . \tag{28}$$

For the present analysis, we use an optical potential of the form

$$U_{op} = -[Vf(r) + iWg(r)] , \qquad (29)$$

where

$$f(r) = [1 + \exp(\frac{r-R_R}{a_R})]^{-1} ,$$

and

$$g(r) = [1 + \exp(\frac{r-R_I}{a_I})]^{-1}$$

with $R_R = r_R A^{1/3}$, $R_I = r_I A^{1/3}$. Thus (28) would have two terms in the derivative and should look like:

$$A_\ell F_\ell(r) = -i^\ell (2\ell + 1)^{-1/2} [\beta_\ell R_R V\frac{df(r)}{dr} + i\beta_\ell R_I W \frac{dg(r)}{dr}]\delta J_f \ell \delta M_f m \qquad (30)$$

Using (30) for the form factor and the expansion of $\chi_f^{(+)}$ into partial waves:

$$\chi_f^{(+)}(\vec{k}_f\vec{r}) = \frac{4\pi}{k_f r} \sum_{LM} i^L \chi_L (k_f r) Y_L^M(\hat{r})Y_L^{M*}(\hat{k}_f) \qquad (31)$$

along with the time reversal relation:

$$\chi^{(-)*}(\vec{k},\vec{r}) = \chi^{(+)}(-\vec{k},\vec{r}) \qquad (32)$$

the $B_{\ell m}$ values may now be determined and the cross sections calculated.

As stated earlier, derivation of the first order vibrational model form factor for even-even nuclei would give a result equivalent to (28). The difference being that β_ℓ

would be interpreted as the root mean square deformation in the ground state due to zero-point oscillations:

$$\beta_\ell{}^2 = \langle \sum_m |\alpha_{\ell m}|^2 \rangle$$

$$= (2\ell + 1)(\hbar\omega_\ell / C_\ell)$$

where $\alpha_{\ell m}$ are the phonon operators of (18), $\hbar\omega_\ell$ is the energy of each phonon, and C_ℓ is the restoring-force parameter.

APPENDIX C

The Method of Coupled Equations

Following the notation of Hillis,[26] the Hamiltonian for the reaction $A(a,a')A'$ is

$$H = T + H(\xi) + V(\vec{r},\xi) \tag{34}$$

where T is the kinetic energy operator of the incident projectile, $H(\xi)$ is the Hamiltonian which describes the internal motion of the target and projectile, and $V(\vec{r},\xi)$ is the total potential describing the interaction between the target and projectile. The coordinates ξ are vector quantities describing the nuclear surfaces of the target and projectile. The Schroedinger equation $H\Psi = E\Psi$ may then be written as

$$[T + H(\xi) + V(\vec{r},\xi)]\Psi(\vec{r},\xi) = E\Psi(\vec{r},\xi) \tag{35}$$

where the energy E is the total energy of the system. As in the solution to the Schroedinger equation presented for the DWBA

$$H(\xi)\psi_\alpha(\xi) = E_\alpha\psi_\alpha(\xi) = (E_a + E_A)\psi_a(\xi_p)\psi_A(\xi_T) \ . \tag{36}$$

Thus, the total energy of the system is

$$E = E_\alpha + \frac{\hbar^2 k_\alpha^2}{2\mu_\alpha} \tag{37}$$

Introduced here is the notation for the entrance channel $\alpha = a + A$. All possible exit channels will be represented as $\alpha' = a' + A'$. Thus $E_\alpha = E_a + E_A$, μ_α is the reduced mass of the system, and k_α is the wavenumber of relative motion.

The solution to the total Hamiltonian may then be written as

$$\Psi(\vec{r},\xi) = \sum_\alpha \psi_\alpha(\xi)\chi_\alpha(\vec{r}) \ , \tag{38}$$

where $\chi_\alpha(\vec{r})$ describes the relative motion of the target and projectile. Multiplying the Schroedinger equation for the total Hamiltonian from the left by $\psi_{\alpha'}^*(\xi)$ and integrating over ξ, one obtains

$$(E - E_\alpha - T)\chi_\alpha(\vec{r}) = \sum_{\alpha=1}^{N} V_{\alpha'\alpha}(\vec{r})\chi_\alpha(\vec{r}) \ , \tag{39}$$

where $\quad V_{\alpha'\alpha}(\vec{r}) \equiv \int \psi_{\alpha'}^*(\xi) V(\vec{r},\xi)\psi_\alpha(\xi)d\xi \ , \tag{40}$

or $\quad V_{\alpha'\alpha}(\vec{r}) = \langle\alpha'|V|\alpha\rangle \ . \tag{41}$

Now, $V_{\alpha'\alpha}(\vec{r})$ may be separated into diagonal-plus-off-diagonal elements so that the Schroedinger equation looks like

$$[E - E_\alpha - T - V_{\alpha\alpha}(r)]\chi_\alpha(r) = \sum_{\alpha \neq \alpha'}^{N} V_{\alpha'\alpha}(\vec{r})\chi_\alpha(\vec{r}) \ . \tag{42}$$

Using separation of variables in a partial wave expansion of χ_α gives

$$\chi_\alpha(r) = \sum_{LM} \frac{U_\alpha(r)}{r} Y_L^M(\Omega) \ . \tag{43}$$

Implicit in this expansion are the assumptions that the incoming projectile may be represented as a plane wave and

that no exchange of nucleons occurs between the target and projectile.

Using (43) in (42), multiplying (42) from the left by $Y_{L'}^{M'}(\Omega')$ and integrating over Ω' gives

$$\int Y_{L'}^{M'}(\Omega') [E - E_\alpha - T - V_{\alpha\alpha}(\vec{r})] \sum_{LM} \frac{U_\alpha(r)}{r} Y_L^M(\Omega) d\Omega'$$

$$= \int Y_{L'}^{M'}(\Omega') \sum_{\substack{\alpha' \neq \alpha \\ LM}}^{N} V_{\alpha'\alpha}(\vec{r}) \frac{U_{\alpha'}(r)}{r} Y_L^M(\Omega) d\Omega' . \qquad (44)$$

The result of this integration gives a set of coupled equations for the radial functions $U(r)$ of the scattered particle for each total angular momentum and parity of the system. For each exit channel α' they have the form

$$[\frac{d^2}{dr^2} - \frac{L_\alpha(L_\alpha+1)}{r^2} + k_\alpha^2 - V_{\alpha\alpha}(r)] U_\alpha(r)$$

$$= \sum_{\alpha' \neq \alpha} V_{\alpha'\alpha}(r) (U_{\alpha'}(r) , \qquad (45)$$

where

$$V_{\alpha'\alpha}(r) = \frac{2\mu}{\hbar^2} \sum_{LM} \int Y_{L'}^{M'}(\Omega) V_{\alpha'\alpha}(\vec{r}) Y_L^M(\Omega) d\Omega . \qquad (46)$$

This equation specifically shows the infinite system of coupled equations which must be solved to determine the wavefunction χ_α. In practice, the number of off-diagonal elements in the coupling potential $V_{\alpha'\alpha}$ is limited to a few of the low lying bound states which compose the majority of the inelastic cross sections, or which are mainly excited by multistep processes. The off-diagonal elements of $V_{\alpha'\alpha}$ correspond roughly with the interaction potential $V(\vec{r}_f, \xi)$ in

the Hamiltonian of equation (1) used to derive the differential cross section in the DWBA analysis of Appendix B.

The diagonal potential $V_{\alpha\alpha}$ is the usual complex optical model (OM) potential describing elastic scattering. However, the elastic scattering is not independent of the off-diagonal matrix elements of $V_{\alpha'\alpha}$ due to the coupling action of the system of equations represented by (47). As shown by (b) in Figure C1, a target nucleus may be excited and undergo a subsequent de-excitation to the ground state while the projectile is still within range of the interaction potential, thus contributing to the elastic cross section. For this reason, elastic and inelastic scattering should be considered simultaneously when searching for an optical model (OM) to describe the elastic scattering process.

The mode of elastic scattering represented by (b) in Figure C1 is not possible in the direct interaction theory used in first order DWBA calculations. To account for this possibility in DWBA, second and possibly higher order terms in the perturbation theory must be employed. The calculations and necessary computer programming, however, become increasingly difficult for additional orders in the Born approximation and this alternative is thus discarded. The coupled channels (CC) method of calculation, which includes these effects, is the best alternative to the standard DWBA method.

The off-diagonal matrix elements of $V_{\alpha'\alpha}$ contain all the information on the inelastic scattering process and therefore
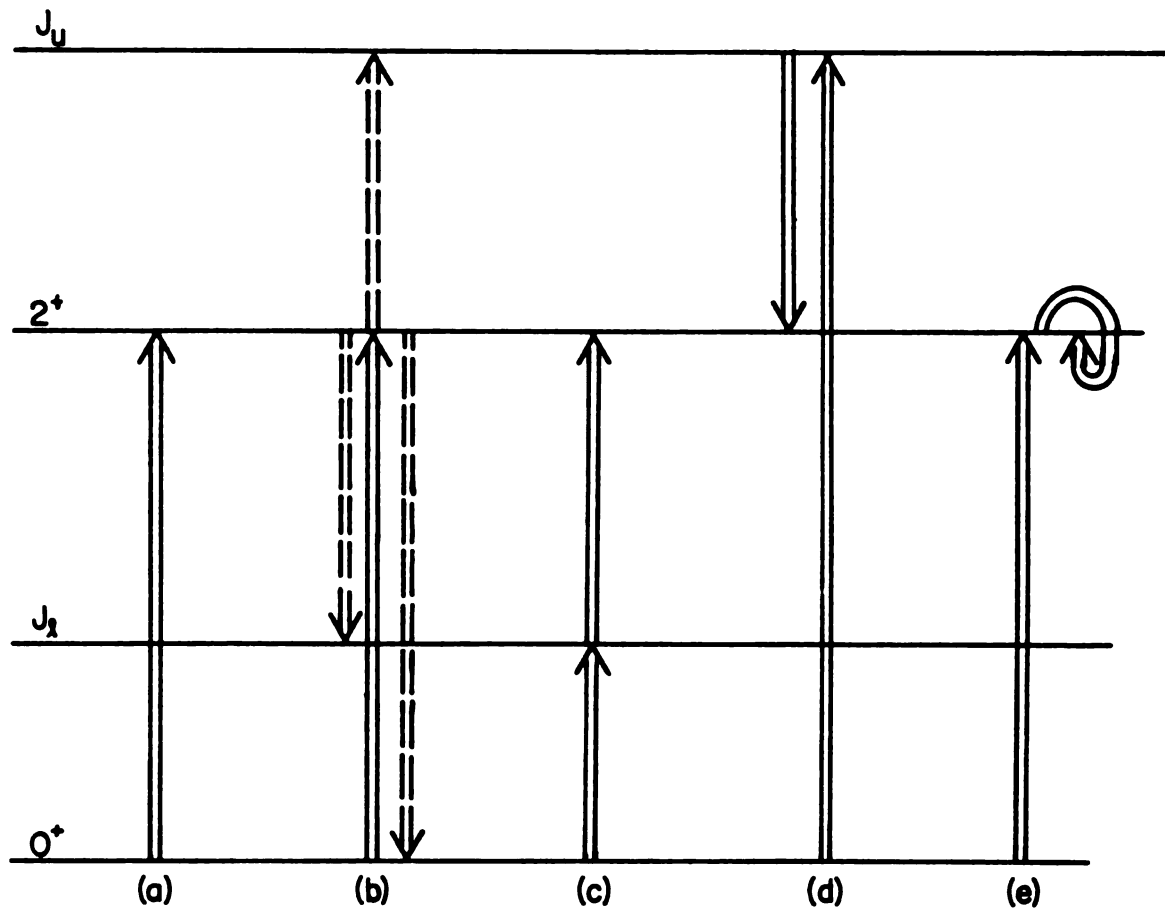
Figure C1. Schematic illustration of the various single and multistep excitation modes included within the coupled channels formalism. The dashed arrows of case (b) illustrate three alternative ways of depopulating the 2⁺ state (from Hillis[26]).

must be chosen very carefully. A mathematical derivation of the matrix elements will not be herein presented, but an in-depth solution is presented by Tamura.[27] Tamura concludes that

$$V_{\alpha'\alpha} = \sum_{t,\lambda} v_\lambda^{(t)}(r) <I||Q_\lambda^{(t)}||I'>A(\ell jI,\ell'j'I',\lambda JS)$$

where $v_\lambda^{(t)}(r)$ contains all the optical model dependence and A is a geometrical factor. The reduced matrix element of $Q_\lambda^{(t)}$ between initial I and final I' spin states contains all the information on nuclear structure. Specifically, $Q_\lambda^{(t)}$ is either the phonon operator of the vibrational model or the multipole moment operator of the rotational model. For example, in the first order vibrational model $Q_\lambda^{(t)}$ is a sum of creation and destruction operators.

As in elastic scattering, the system of coupled equations represented by (46) gives rise to inelastic transitions which occur via multistep processes and cannot be calculated with standard DWBA techniques. Examples of this type of transition are represented schematically in (b)−(e) of Figure C1. Multistep processes of this type are most important in nuclei which exhibit strong collective natures in the low lying levels. Specifically, the higher phonon states of the vibrational nuclei and the higher angular momentum states of rotational nuclei are the most likely to be affected.

Another contribution which is more often important in heavy ion scattering is the "reorientation" effect. The

incoming projectile excites a given state in the target nucleus. Then, while still within range of the interaction potential, it causes a reorientation or change in the rate of precession of the nuclear spin vector. This process is represented schematically by (e) of Figure C1.

The method of coupled channels thus gives a more accurate representation of the interaction mechanisms between target and projectile for nuclear bands with strongly collective natures. The standard DWBA is still a good description when used as intended: to explain transitions to excited states that occur primarily through single step processes.

LIST OF REFERENCES

LIST OF REFERENCES

1. L.T. Chua, F.D. Becchetti, J. Janecke and F.L. Milder, Nucl. Phys. A273, 243 (1976).

2. R.I. Cutler M.J. Nadworny, and K.W. Kemper, Phys. Rev. C15, 1318 (1977).

3. R.J. Puigh and K.W. Kemper, Nucl. Phys. A313, 363 (1979).

4. K.W. Kemper, A.F. Zeller, T.R. Ophel, D.F. Hebbard, A. Johnston, and D.E. Weisser, Florida State University, to be published.

5. R. Huffman, A. Galonsky, C. Williamson, and R. Markham, Michigan State University, to be published.

6. B. Buck, Phys. Rev. 127, 940 (1962).

7. Daniel J. Horen, J.R. Meriweather, B.G. Harvey, A.B. de Nercy, and J. Mahoney, Nucl. Phys. 72, 97 (1965).

8. R. Pardo, R. Markham, W. Benenson, A. Galonsky, and E. Kashy, Phys. Lett. 71B, 301 (1977).

9. E.D. Hudson and M.L. Mallory, Nucl. Sci. NS-23, 1065 (1976).

10. P.S. Miller, H. Laumer, M.L. Mallory, and J.A. Nolen, Jr., Proceedings of Particle Accelerator Conference of March 1979 in San Francisco, CA, to be published in Proceedings of IEEE Transactions in Nuclear Science June 1979.

11. L. Robinson, Annual Report of the Michigan State University Cyclotron Laboratory, 1977–78.

12. P.D. Kunz, University of Colorado, (unpublished).

13. J. Raynal, Centre d'Etudes Nucleaires de Saclay, (unpublished).

14. D.L. Hillis, E.E. Gross, D.C. Hensley, C.R. Bingham, F.T. Baker, and A. Scott, Phys. Rev. C15, 1467 (1977).

15. N. Lingappa and G.W. Greenlees, Phys. Rev. C$\underline{2}$, 1329 (1970).

16. D.A. Goldberg, S.M. Smith, H.G. Pugh, P.G. Roos, and N.S. Wall, Phys. Rev. C$\underline{7}$, 1938 (1973).

17. R.H. Bassel, G.R. Satchler, R.M. Drisko, and E. Rost, Phys. Rev. $\underline{128}$, 2693 (1962).

18. H.W. Broek, J.L. Yntema, B. Buck, and G.R. Satchler, Nucl. Phys. $\underline{64}$, 259 (1965).

19. G.R. Satchler, Nucl. Phys. $\underline{70}$, 177 (1965).

20. S.A. Fulling and G.R. Satchler, Nucl. Phys. $\underline{A111}$, 81 (1968).

21. C. Michael Lederer and Virginia S. Shirley, Table of Isotopes, Seventh Edition, John Wiley & Sons, New York, 1978, pp 170-171.

22. D.A. Goldberg and S.M. Smith, Phys. Rev. Lett. $\underline{29}$, 500 (1972).

23. R.R. Doering, A.I. Galonsky, R.A. Hinrichs, J. of Comp. Phys. $\underline{12}$, 498 (1973).

24. N. Austern in Selected Topics in Nuclear Theory, IAEA, Austria, 1964.

25. G.R. Satchler in Lectures in Theoretical Physics, Vol. 8C, University of Colorado Press, Boulder, 1966.

26. D.L. Hillis, Ph.D. Thesis, University of Tennessee, 1976 (unpublished).

27. T. Tamura, Rev. of Mod. Phys. $\underline{37}$, 679 (1965).